TECHNIQUES TO IDENTIFY THE MAGNETIC SUSCEPTIBILTY OF SUBCELLULAR ORGANELLES: A FEASIBILITY ANALYSIS

A THESIS
SUBMITTED TO THE FACULTY OF THE GRADUATE SCHOOL
OF THE UNIVERSITY OF MINNESOTA
BY

Emily Stewart Paukert

IN PARTIAL FULFILLMENT OF THE REQUIREMENTS
FOR THE DEGREE OF
MASTER OF SCIENCE

Professor Susan Mantell

November 2010

Abstract

Magnetic susceptibility is the degree of magnetization in response to an applied magnetic field. While the expected magnetic susceptibility of subcellular components is on the order of 9.05×10^{-6}, variations in subcellular magnetic susceptibility as low as 10% can create forces in the pN range within a cell when high intensity magnetic fields are imposed. The objective of this study is to investigate the feasibility of two techniques to measure the magnetic susceptibility of subcellular organelles. The sensitivity and accuracy of resonance frequency shifts of microcantilever beams and magnetophoresis are evaluated to ensure magnetic susceptibility measurements can be obtained within the expected range for subcellular organelles.

The resonance frequency detection method was tested using a bismuth particle and permanent magnets ($B*dB/dz = 0.54\ T^2/m$) to determine an uncertainty of 0.013 Hz. To determine the technique feasibility for application to subcellular organelles, a theoretical examination of resonance frequency shifts due to the application of magnetic field and gradient products varying from $0.54\ T^2/m$ (permanent magnets) to $1300\ T^2/m$ (superconducting magnet) was conducted for silicon, silicon nitride and polymer beams of varying dimensions. Results indicate that only a polymer beam can produce a detectable resonance frequency shift that is greater than the experimentally determined uncertainty. However, an uncertainty smaller than 0.009 Hz is required to sense the differences in resonance frequency shifts due to a 10% variance in magnetic susceptibility. In summary, the microcantilever beam approach cannot achieve sufficient sensitivity to detect the predicted differences among different subcellular organelle types.

Tests implementing magnetophoresis for polystyrene test particles with a 100 μm diameter explored the sensitivity and accuracy effects of varying fluid flow speeds of 0.63, 1.09, and 1.44 mm/sec, different particle radius to channel depth ratios (r/a) of 0.043 and 0.199, and a magnetic field and gradient product ($B*dB/dz$) of 38.91 T^2/m. Particle speed due to the magnetic field was recorded by a CCD camera with 32.68 pixels/mm resolution. The percent uncertainties of the experimental magnetic susceptibilities are 12.3, 18.3 and 22.4% (in order of flow speed). The trial runs were also used to determine that the smallest detectable magnetic velocity for the detection method is 3.16 ± 15 μm /sec and the smallest detectable particle diameter is 31 μm. The trial runs indicate that a balance of a larger r/a ratio and a slower flow speed is ideal to optimize consistency in flow velocities and calculated magnetic susceptibilities while minimizing uncertainty. A theoretical examination of organelle magnetic velocities due to the application of magnetic field and gradient products of -38.91 T^2/m and -1300 T^2/m indicates that the nuclei and large mitochondria are detectable in either magnetic field while the small mitochondria is detectable only in the larger magnetic field. In addition, all organelles have diameters smaller than 31 μm rendering them undetectable by the current visualization method. The following recommendations are necessary to detect the magnetic susceptibilities of subcellular organelles through magnetophoresis with sufficient accuracy: use the larger $B*dB/dz$ (-1300 T^2/m), reorient the channel or incorporate a level so that gravity is not a factor, and use a higher quality velocity detection method.

Table of Contents

List of Tables

List of Figures

Nomenclature

F_{mag}	N	magnetic force
χ	m^3/kg	magnetic susceptibility
μ_0	4π x10^{-7} N/A^2	vacuum permeability
B	T	magnetic field strength
dB/dz	T/m	magnetic field gradient
$\overline{\chi}$	-	dimensionless magnetic susceptibility
ρ	kg/m^3	density
f_0	Hz	resonance frequency of a microcantilever beam
m_b	kg	mass of the beam
k	kg/sec^2	beam stiffness
E	Pa	modulus of elasticity
I	m^4	moment of inertia
L	m	length of the beam
f_s	Hz	resonance frequency of a beam with a sample on the tip
m_s	kg	mass of the sample
$\delta F/\delta z$	N/m	magnetic force gradient
$f_{s,m}$	Hz	resonance frequency of a beam with a sample on the tip in a magnetic field
h	m	distance between the two permanent magnets
z_0		location of the microcantilever beam
M	A/m	magnetization , magnetic moment per unit volume
a_0	-	point at which magnetic field measurement is taken to calibrate COMSOL
a_1	m	distance at which permanent magnet field goes to zero, used to calibrate COMSOL
b	m	beam width
t	m	beam thickness

σ	-	standard deviation
U	-	uncertainty, twice the standard deviation
U_{xf}	m/s	flow velocity
U_{zf}	m/s	displacement velocity due to the magnetic force
F_D	N	viscous drag force
F_g	N	gravitational force
Φ	radians	offset angle between the x_f-z_f and x-z coordinate systems
$\overline{\chi}_{fl}$	-	dimensionless magnetic susceptibility of the fluid
V_p	m^3	volume of a test particle
η		viscosity
r	m	particle radius
C_w	-	viscous drag coefficient
a	m	channel depth
C_{w1}	-	viscous drag coefficient for a particle located at the center of the channel ($y = 0$)
C_{w2}	-	viscous drag coefficient for a particle located a distance of one third of the channel depth away from a wall ($y = a/6$)
C_{w3}	-	viscous drag coefficient for a particle located a distance of a_3 from a wall
a_3	m	length scale used to calculate C_{w3}; distance from nearest wall
$\overline{\chi}_1$	-	published polystyrene magnetic susceptibility value -8.21×10^{-6} (Tarn et al., 2009)
$\overline{\chi}_2$	-	published polystyrene magnetic susceptibility value -1.02×10^{-6} (Tanimoto et al., 2005)
p	-	weight fraction
R^2	-	coefficient of determination
U_{f0}	m/s	velocity vector outside of magnet

θ_0	radians	angle between the velocity vector U_{f0} and the x_c-axis
U_c	m/s	velocity vector in the x_c-z_c coordinate system
θ_m	radians	angle between the velocity vector U_c and the x_c-axis
$\overline{C}_{w12}$	-	average of C_{w1} and C_{w2}
$\overline{C}_{w23}$	-	average of C_{w2} and C_{w3} ($l_3 = a/4$)
l	m	length of the flow channel
Δp		pressure gradient
U_{xmax}	m/s	maximum fluid velocity for flow between two parallel plates
U_{xt}	m/s	fluid velocity at a distance of one third of the channel width from the wall for flow between two parallel plates
U_{avg}	m/s	average fluid velocity for flow between two parallel plates
Re	-	Reynolds number

1. Introduction

1.1 Motivation

Cellular mechanical stimulations have been shown to produce biological and chemical responses within a cell. As a result, the effect of stresses and strains on individual cells has received increasing attention from researchers.

The mechanical properties of cells have been explored as a first step to understanding the conversion of mechanical modifications to cellular responses through theoretical models and experimental manipulation of live cells. In their 2006 review paper, C.T. Lim et al. document a large body of recent work on mechanical models of cellular behavior in response to transient and dynamic loads. A collection of continuum approach models that treat an individual cell as one uniform body have achieved reasonable success in predicting general mechanical deformation of living cells. For example, the Newtonian liquid drop model that treats the interior of the cell as a homogeneous Newtonian viscous liquid with viscosities varying from 100 to 200 Pa·sec and the exterior as an anisotropic viscous fluid layer with surface tensions varying from 0.02 to 0.04 $x10^{-3}$ N/m has compared favorably to experiments for a variety of cell types. J.J.W.A. van Loon (2007) outlines a variety of force application methods to examine live cell behavior. Cell responses to forces ranging from 1pN to 500μN due to cell poking, tensile stretching, pressure, fluid shear stress, and vibration have been studied to characterize cell behavior.

Stresses and strains can produce a variety of internal cellular changes. For example, extracellular fluid shear of endothelial cells activates hormone release and causes cell stiffening due to cytoskeleton rearrangement (Lim et al., 2006). While cells are most commonly exposed to internal physiologically related forces like the fluid shear of endothelial cells due to blood flow, external environmental forces have been investigated as well, gravity in particular. Gravity is a weak force relative to the weak nuclear force, electromagnetic force, and the strong nuclear force that dominate the force field within and between molecules inside a cell. The relative ratio of strong nuclear to electromagnetic to weak nuclear to gravity is approximately 1: 10^{-2} : 10^{-5} : 10^{-39}. However, gravity has been shown to directly impact single cells in space flight microgravity experiments. For example, an increase in force from 1 to 3 g's has produced cellular shape changes (J.J.W.A. Loon, 2007). The impact of gravitational forces on bone cells in particular has garnered special attention. The specialized process through which bone tissue adapts to mechanical usage and external forces such as weight and gravity, estimated to be on the order of 1 pN on the cellular level, has proved an interesting challenge for researchers (Cowin, 1998). While the adaptive ability of bone tissue provides an environmental advantage, often changes to the mechanical properties of cells can be detrimental. For example, malaria-causing single-cell parasites cause stiffening to the red blood cell membranes. As a result, the red blood cells can no longer deform through blood vessels and narrow capillaries thereby greatly impeding blood flow which can be deadly (Lim et al., 2006).

Due in part to the increasing prevalence of MRI usage, understanding the effect of high intensity magnetic fields on the cellular level is significant. If different subcellular

components react to the magnetic field in differing ways, potentially detrimental internal cell stresses could occur. In addition, understanding of the magnetic properties of subcellular components could be used to target and elicit a specific cellular response as magnetic therapy.

1.2 Research Objectives

The objective of the present study is to develop a technique to measure the magnetic susceptibility of subcellular organelles. The sensitivity and accuracy of the technique must be evaluated to ensure measurements can be obtained within the expected range for subcellular organelles.

2. Literature Review

Magnetic susceptibility is the degree of magnetization of a material in response to an applied magnetic field. The magnetic force F_{mag} (N) is a function of the magnetic susceptibility χ (m^3/kg), the vacuum permeability μ_0 ($4\pi x10^{-7} N/A^2$), the magnetic field B (T), the magnetic field gradient dB/dz (T/m) and the mass m (kg) of the sample of interest

$$F_{mag} = \frac{\chi m B}{\mu_0}\frac{dB}{dz}. \tag{2.1}$$

Equation 2.1 is often rewritten in terms of the dimensionless magnetic susceptibility $\overline{\chi}$ which is the product of the magnetic susceptibility and the density ρ

$$\overline{\chi} = \rho\chi. \tag{2.2}$$

Materials can be either diamagnetic or paramagnetic. In diamagnetic materials, the orbital velocity of electrons around their nuclei changes in response to an external magnetic field causing the magnetic dipole moment to be oriented in the direction opposing the field. As a result, the material experiences a repulsive effect due to the external magnetic field meaning the magnetic susceptibility is negative. Magnetic susceptibilities are known for various diamagnetic elements such as water, $-9.051x10^{-9}$ m^3/kg, and bismuth, $-1.70x10^{-8}$ m^3/kg. In contrast, paramagnetic materials have a positive magnetic susceptibility and experience an attractive effect. Both effects are difficult to observe since the diamagnetic and paramagnetic properties are relatively weak. While magnetic susceptibilities are known for many elements and materials, there has been very little exploration into the magnetic susceptibility of biological specimens.

The magnetic properties of cells are of particular interest due to the potential internal stresses inflicted on the cell in a magnetic field. Detection of the magnetic susceptibility of internal cellular components or subcellular organelles presents a unique challenge for various reasons. Since the magnetic force is proportional to the magnetic susceptibility as well as the mass of the organelle, it is important to accurately know the mass. In addition, the small size makes it difficult to visually detect the organelle response to a magnetic field. The detection of magnetic susceptibility is also difficult since the magnetic susceptibility is expected to be quite small. Furthermore, the magnetic susceptibility variance between organelle types is expected to be small as well (about 10%). As a result, the detection technique must be extremely accurate.

To evaluate any technique for feasibility, basic attributes of subcellular organelles must be identified. Figure 2.1 shows a diagram of the cell and details all of the subcellular organelles such as ribosomes, mitochondria, and nuclei. Cells of different types vary in size and consequently subcellular organelles vary in size as well. Mitochondria are between 1 and 10 micrometer in diameter while ribosomes are typically 20 nanometers. The nuclei are largest and vary between 11 and 22 micrometers. The mass and mass density of subcellular organelles is unknown and currently immeasurable, however it is reasonable to treat the organelles as spheres with the aforementioned diameters and the density of water, thereby enabling an estimate of mass, detailed in Table 2.1 (Cowin, 1998). The mass estimates vary from 4.19×10^{-21} kg (ribosome) to 5.58×10^{-12} kg (large nuclei). It is also assumed that extracting the organelles from their natural environment does not have an affect on the experimental magnetic susceptibility. In addition, it is assumed that the magnetic susceptibility of the subcellular organelles is

approximately equal to that of water with a 10% variance between organelle types. The differences in subcellular organelle size and magnetic susceptibility can produce force differentials on the order of 1pN in the presence of high intensity magnetic fields. Figure 2.2 plots magnetic force against the product of magnetic susceptibility and particle volume for the different subcellular organelles. The vertical black lines represent the subcellular organelle magnetic force results for a magnetic susceptibility of -9.051×10^{-9} m^3/kg while the shaded region indicates the effects of a ±10% difference in magnetic susceptibility. In addition, five magnetic field and gradient products are plotted for reference. Permanent magnets can produce field and gradient products of $10 T^2/m$, while a variety of superconducting magnets are necessary to produce the much larger products. The field and gradient product of 10 T^2/m produces a force differential of 0.4 pN between the large nuclei and the small mitochondria while the product of 50 T^2/m produces a differential of 2 pN.

Magnetic susceptibility is commonly measured using the basic principle that the weight of the sample increases or decreases proportionally to the magnetic susceptibility when placed (with the correct orientation) in a magnetic field. Different scales varying from a rudimentary conventional laboratory balance to a more sophisticated version that outputs the magnetic susceptibility have been used to measure magnetic susceptibility. However, even a more sophisticated version like the MK1 manufactured by Sherwood Scientific, Ltd. requires at least 250mg of the sample of interest to make an accurate measurement, meaning extremely large numbers of subcellular organelles (i.e. 4.47×10^7 large nuclei) would be needed. As such, the benefits of other techniques must be examined.

Two different techniques, magnetophoresis (Section 4) and a vibrating microcantilever beam (Section 3), will be examined in this paper to determine if either can detect the magnetic susceptibility of subcellular organelles with sufficient accuracy. A basic description and a literature review pertaining to the specific techniques are included in Section 3.1 (microcantilever beam) and Section 4.1 (magnetophoresis).

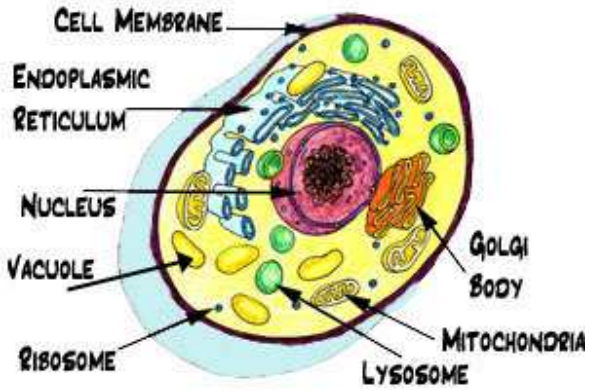

Figure 2.1 – Cell diagram and its internal components (ColonCancerResource.com)

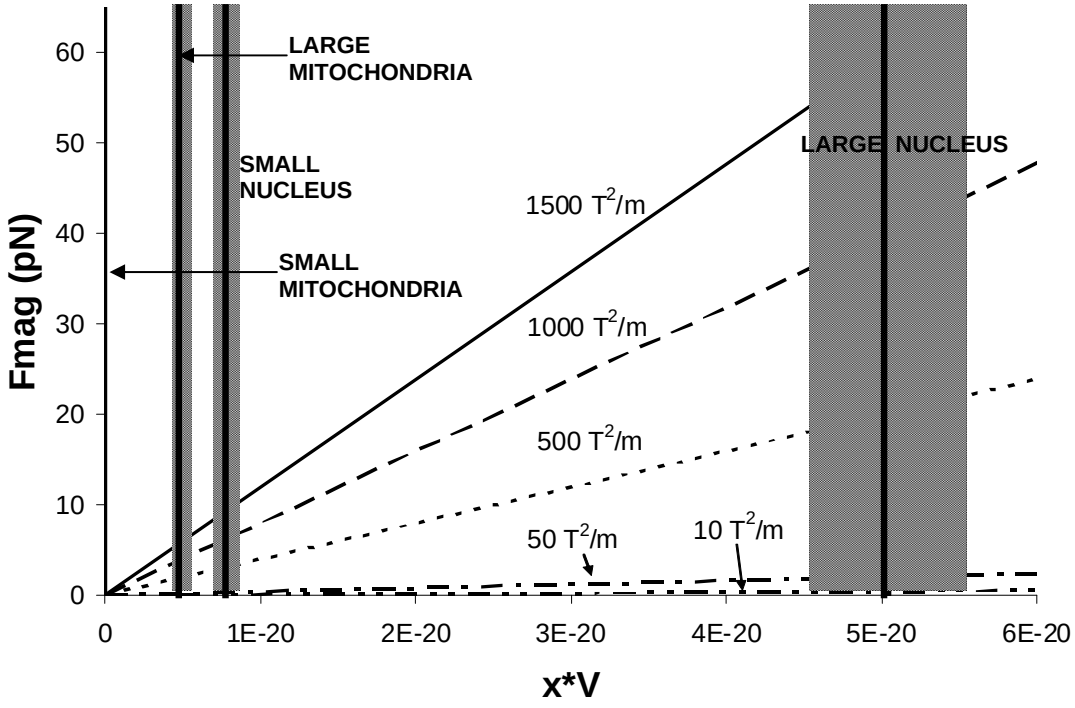

Figure 2.2 – An illustration of the relationship between magnetic force and the product of particle magnetic susceptibility and volume for different magnetic field and gradient products. The magnetic forces of subcellular organelles for magnetic susceptibilities of 9.05×10^{-6} are included as well as the expected range of ± 10%.

Table 2.1 - Sizes and estimated masses of the subcellular organelles to be used in the analysis

Subcellular Organelle	Diameter (μm)	Volume (m^3)	Mass (kg)
small mitochondria	1	5.24E-19	5.24E-16
large mitochondria	10	5.24E-16	5.24E-13
ribosomes	0.02	4.19E-24	4.19E-21
small nuclei	11	6.97E-16	6.97E-13
large nuclei	22	5.58E-15	5.58E-12

3. Microcantilever Beam

3.1 Background

Microcantilever beams can be very useful as a sensor to evaluate the effects different types of physical, chemical, or biological stimuli. The stimulus causes modifications to beam mass and/or stiffness which results in a change in static deformation and/or resonance frequency. The concept has been used to sense the presence of particular gases, chemicals, and biological species as well as in the study of long-term mechanical performance of MEMS (Calleja et al., 2005; Lavrik et al., 2004; Ali et al., 2007). Microcantilever beam sensors have been used to measure the magnetic susceptibility of nanogram quantities of materials (Finot et al., 2001). The general approach involves placing particles on a beam tip and subjecting the beam to a magnetic field. Beam displacement or a resonance frequency shift is measured and used to evaluate magnetic susceptibility. The study presented in Finot et al. successfully used the resonance frequency technique to measure the magnetic susceptibility of various paramagnetic samples such as iron sulfate and stainless steel with masses varying from 1.1 to 15.7 ng. The magnetic susceptibilities varied from 6.35×10^{-9} to 2.33×10^{-7} m^3/kg (see Appendix A for further analysis). Since the technique has been used to reach a similar objective, the approach appears promising. The approach does not involve any visual sensing of the subcellular organelles beyond the placement on the beam tip, the beam dimensions and material can be modified to make the system more sensitive, and it is possible to clump multiple organelles together on the tip to magnify the effect.

However, it is still unknown if the accuracy of the technique is sufficient to detect the small resonance frequency changes that is expected for subcellular organelles. In addition, there many unique challenges to designing a vibrating microcantilever beam apparatus that senses changes in resonance frequency and can be placed in the bore of a superconducting magnet. As such, the technique is currently limited to the application of a magnetic field and gradient from permanent magnets. The following sections discuss the theory behind the vibrating microcantilever beam technique and an experimental trial run that seeks to address the previously mentioned challenges.

3.2 Theory

The resonance frequency of a cantilever beam is a function of the beam stiffness k (kg/sec^2) and mass m (kg)

$$f = \frac{1}{2\pi}\sqrt{\frac{k}{m}}\,. \tag{3.1}$$

If the beam mass is considered distributed along the length of the beam, the resonance frequency of a beam f_0 (Hz) can be calculated using Equation 3.2

$$f_0 = \frac{1}{2\pi}\sqrt{\frac{k}{0.236m_b}} = \frac{1}{2\pi}\sqrt{\frac{3EI}{0.236m_bL^3}} \tag{3.2}$$

where m_b (kg) is the mass of the beam, E (Pa) is the modulus of elasticity, I (m^4) is the moment of inertia, and L (m) is the length of the beam. The mass or stiffness of the beam will change when samples are added to the tip or the beam sample if vibrated in a magnetic field. The resonance frequency of a beam with a sample on the tip f_s can be calculated using Equation 3.3

$$f_s = \frac{1}{2\pi}\sqrt{\frac{k}{m_s + 0.236m_b}} \tag{3.3}$$

where m_s (kg) is the mass of the sample.

When the beam with a sample is placed in a magnetic field, the magnetic field will affect the effective stiffness of the beam and mass system. The resonance frequency of the beam with a sample on the tip and in a magnetic field $f_{s,m}$ is

$$f_{s,m} = \frac{1}{2\pi}\sqrt{\frac{k + \frac{\partial F}{\partial z}}{m_s + 0.236m_b}} \tag{3.4}$$

where $\delta F/\delta z$ (N/m) is the magnetic force gradient acting on the sample (Finot et al., 2001).

To ensure a detectable frequency shift between f_s and $f_{s,m}$, k and dF/dz must be of similar magnitude. The magnetic force gradient can be calculated by taking the derivative of Equation 2.1 with respect to z

$$\frac{dF}{dz} = \frac{\chi m_s}{\mu_0}\left[\left(\frac{dB}{dz}\right)^2 + B\frac{d^2B}{dz^2}\right]. \tag{3.5}$$

Since the mass of a single subcellular organelle, m_s, is unknown, the mass is approximated using the beam stiffness and resonance frequencies

$$m_s = \frac{k}{4\pi^2 f_s^{\,2}}\left(1 - \frac{f_s^{\,2}}{f_o^{\,2}}\right). \tag{3.6}$$

Equations 3.3-3.6 are combined to find the magnetic susceptibility

$$\chi = \frac{4\mu_0\pi^2}{\left(\frac{dB}{dz}\right)^2 + B\frac{d^2B}{dz^2}} \frac{f_s f_0^{\,2}(f_{s,m} - f_s)}{f_o^{\,2} - f_s^{\,2}} \quad . \tag{3.7}$$

In Equation 3.7, f_0, f_s, and $f_{s,m}$ are measured using a vibrating microcantilever beam in a magnetic field with a known magnetic field and gradient. The following sections will evaluate the feasibility of the resonance frequency shift method to determine if the small magnetic susceptibility differences between subcellular organelle types can be discerned.

3.3 Method

In order to evaluate the feasibility of the technique, various unknowns must be resolved. The magnetic field gradients of available magnetic field sources must be characterized to estimate potential frequency shifts using Equations 3.3-3.5 and to calculate χ from Equation 3.7. The sensitivity of the frequency detection method must also be characterized so that the accuracy capability is known and to determine if the expected frequency shifts can be detected. The following sections detail the methods for characterizing the magnetic field produced by two permanent magnets, resonance frequency detection, and uncertainty determination.

Magnetic Field Characterization

Readily available magnetic field sources include Neodymium permanent magnets (K&J Magnetics, BX084-N52) and a superconducting 17T magnet (Center for Interdisciplinary Applications in Magnetic Resonance). The superconducting magnet is well-characterized with a maximum gradient of 100 T/m at B = 13 T. However, the magnetic field distribution is unknown for the field produced by the two permanent magnets. The permanent magnets were aligned to repel with a central distance h of 5

millimeters (see Figure 3.1). Each magnet has dimensions 2.54 x 1.27 x 0.635 cm. The dimension z_0 indicates the location of the microcantilever beam.

The Neodymium permanent magnets were studied using the Matlab-based COMSOL finite element analysis program. The study allowed for an estimate of *B* and *dB/dz* at the location of the sample on the tip of a beam using magnetostatic modeling. In addition, COMSOL enabled an exploration of the benefits of different magnet positions since the field and gradient are dependent on the magnet positions.

A 3-Dimensional drawing of the magnets was created in COMSOL (see Figure 3.1) with the above specified dimensions and a surrounding sphere to define the solution space with a radius of 5 cm. The magnets were assigned a library material of 'soft iron without losses.' The surrounding sphere was used as a boundary condition at which there is zero potential and contains air. A fine mesh was created and used to solve for the 3D magnetic field. An additional COMSOL input, the magnetization *M* (magnetic moment per unit volume) is unknown for these particular magnets. The magnetization of the magnets was adjusted until the COMSOL output produced a magnetic field matching measurements taken at two points. A Gauss meter (F.W. Bell, model # 5180) was used to measure the field strength (0.1 T) at the top surface between the two magnets on the z-axis at location a_0. In addition, the distance along the z-axis at which the field goes to zero, a_1, was measured (3.5 cm).

Frequency Detection Characterization

The frequency detection method used in this study allows manipulation of a stack PZT to actuate the microcantilever beam (Ali et al., 2006; Kuehn et al., 2007). A laser

beam is reflected off of the tip of the beam onto a photosensitive diode (PSD) device. As shown in Figure 3.2, a LabVIEW program runs a frequency sweep signal to the beam and the PSD signal is recorded. The resonance frequency is found at the center of a Gaussian Peak fit to the data. The LabVIEW VI allows the user to set the sampling rate as well as the size and location of the frequency sweep. The beam, sample and magnetic force positioning are detailed in Figure 3.3.

To characterize the sensitivity of the system, four silicon test beams with different resonance frequencies were used. The silicon beams were constructed with a length L of 5 mm, width b of 2 mm, and a thickness t between 20 and 50 μm (see Figure 3.3). While the exact thickness is not known due to construction techniques the beam stiffness can be calculated from the resonance frequency. Three of the beams were used to run approximately one hundred consecutive frequency sweeps on three separate occasions for each beam to obtain an array of resonance frequency values. The uncertainty U is characterized by obtaining the standard deviation σ of the data where $U=2\sigma$. Three averages and standard deviations were calculated from the three data sets for each beam and then averaged to obtain the final experimental resonance frequency and uncertainty estimates. Additionally, a test sample of bismuth, chosen for its relatively high magnetic susceptibility, was used to study the effect of the magnetic field**.** A sample of relatively large size was obtained to maximize the magnetic response. The sample was glued to the tip of the fourth silicon microcantilever beam. The current system is not compatible with the superconducting magnet so only the permanent magnets were used in the experiment.

3.4 Results

The magnetic field modeling results and uncertainty calculations are discussed in detail in the following sections.

Magnetic Field Characterization

A magnetization *M* of 250,000 A/m produces a 3D magnetic field that correlates to the two measured calibration values. The 3D magnetic field COMSOL output was used to create a plot of the magnetic field in the z-direction along the z-axis (Figure 3.4). The COMSOL solution data was imported into Excel and used to create a trendline of the data from z = -0.04 m to the maximum peak at approximately z = -0.0127 m. The derivative of the trendline at z = -0.0165 m (the location of the beam, where z_0 = 3.8mm) yields a gradient of 10.7 T/m. The equation indicates a magnetic field of 0.05 T at the location of the beam.

Frequency Detection Characterization

Table 3.2 details the experimental results. The average resonance frequencies with calculated uncertainties as determined by the frequency detection system are 151.77, 248.00, and 679.00 listed for the three silicon beams, respectively labeled 1, 2, and 3. The average uncertainty is 0.013 Hz. The table also lists the averaged resonance frequency results for the silicon beam with an attached bismuth sample with and without a magnetic field. Resonance frequency sweeps measured resonance frequencies of approximately 155 Hz for both cases. There was no detectable difference when the beam and mass system was placed in the magnetic field.

It should be noted that during experimental evaluation the frequency detection method frequency measurements were very sensitive to air movement and temperature changes.

3.5 Analysis and Discussion

The following section analyzes the significance of the magnetic field and frequency detection method characterization results as well as the implications of the results on the feasibility of the technique to identify the magnetic susceptibility of subcellular organelles.

Magnetic Field Optimization

Since the current system detailed in Figure 3.2 is only compatible with permanent magnets, it is desirable to maximize the magnetic field and gradient at the location of the beam for the permanent magnets. Different magnet positions result in different distributions that can easily be explored using COMSOL. The magnetic field and gradient can be maximized by moving the magnets together so that h=0 mm. Figure 3.5 compares the magnetic fields for the two situations.

Using the same approach as discussed previously, there is a magnetic field of 0.054 T and a gradient of 17 T/m for h= 0mm and z_0 = 3.8mm. These values indicate a 8% increase in magnetic field and a 58% increase in the gradient as a result of decreasing h to zero. If the beam is moved 2 mm closer to the magnets (h = 0, z_0 =1.8mm), the gradient becomes 143 T/m with a field of 0.08T. The result is a 60% increase in

magnetic field and a 1236% increase in the gradient. This increased field and gradient will be considered in evaluating whether the purposed technique is feasible.

Frequency Detection Optimization

The variations in uncertainties in Table 3.2 can, at least in part, be explained by the differences in stiffness *k*. For less stiff beams, those with smaller *k* values, the frequency sweep peak becomes flattened due to damping effects (Figure 3.5). As a result, the experimentally determined resonance frequency value becomes less accurate since the peak (located at the resonance frequency) is less well defined.

Although the uncertainty will vary due to *k*, it is useful to average the uncertainties found in Table 3.2 for analysis purposes. An average of 0.013 Hz gives an estimated uncertainty against which expected frequency shifts can be evaluated.

It is useful to compare the experimental results obtained with a bismuth sample and permanent magnets to the theoretical predictions that result from the equations and magnet modeling to verify the authenticity. The resonance frequency of the silicon beam with the bismuth sample on the tip with or without a magnetic field is 155 Hz. From the dimensions of the beam (L=5mm, b=2mm, t=50 μm) and the density of silicon (2,330 kg/m^3), the mass of the beam is estimated to be 1.17×10^{-6} kg. Using the beam material characteristics and dimensions, a theoretical value of 75.0 N/m is obtained for *k*. Using all of the above values along with Equation 3.3, the mass of the bismuth sample is estimated to be 7.88×10^{-5} kg. Using the COMSOL modeling, a magnetic field and gradient product of 7.72 T^2/m is estimated. From the field and mass estimates, the force gradient estimate is 7.82×10^{-5} N/m (Equation 3.5). Therefore, using Equation 3.4, the

theoretical prediction for $f_{s,m}$ is 154.9988 Hz. The expected shift due to the magnetic field is 0.0012 Hz. This prediction matches to the observed experimental results since no noticeable shift was observed and the vibration technique was evaluated to only be sensitive to 0.013 Hz.

Subcellular Organelle Feasiblity

The field and sensitivity characterizations allow for feasibility evaluation of different microcantilever beam and magnetic field source possibilities. As evidenced by Equation 3.4, the choice of beam material and dimensions has a large impact on the results. Due to the relationship in Equation 3.5, *dF/dz* will be quite small, even for large values of *dB/dz*. As a result, it would appear that a beam with a small *k* would be ideal to obtain a detectable shift. However, if the beam is too flexible, the resonance frequency estimate will be less accurate and harder to identify due to damping effects.

For analysis purposes, it is useful to discuss and define the characteristics of three typical microcantilever beam materials, polymer, silicon, and silicon nitride, with dimensions ranging from 0.1 μm thick and 200 μm long (polymer) to 500 μm thick and 3000 μm long (silicon), see Table 3.3. The values of *k* vary from 4.38×10^{-6} (polymer) to 174 kg/sec^2 (silicon).

In addition to the assumptions made about subcellular organelles in section 2, a theoretical estimate of the number of subcellular organelles that could be clustered and placed on the tip of the beams is necessary to the analysis process. It is assumed that the organelles would be clumped to form a sphere with a diameter equal to that of the width of the beam. It is also assumed that 50% of the volume of the clumped sphere is void.

To calculate the number of subcellular organelles, 50% of the volume of a sphere with the diameter of the width of the beam is divided by the volume of an individual subcellular organelle. The numbers of organelles that can be clumped together to fit on a beam tip vary from 47 (large nuclei) to 62,500 billion (ribosomes). All results are shown below in Table 3.4.

Since the volume of each subcellular organelle type being placed on the beam is equal as well as the assumed density and magnetic susceptibility (for current calculations), the resonance frequencies and shifts are equal for every type of subcellular organelle. The frequency shifts ($f_{s,m} - f_s$) due to the different permanent magnet positions and the superconducting magnet are in Table 3.5.

Evaluating against the experimentally determined 0.013 Hz uncertainty, only a polymer beam in the superconducting magnet or near the 143 T/m gradient from permanent magnets would produce detectable results. This conclusion is demonstrated visually in Figure 3.5.

However, the 0.013 Hz uncertainty was evaluated for a silicon beam. Due to the smaller k of the polymer beam, it is likely that the damping effect would be large and generate a flatter frequency sweep making the resonance frequency harder to identify accurately resulting in a much larger uncertainty.

Now that the possible beam and magnet choices have been identified, it is possible to explore the effect of a 10% variance in magnetic susceptibility. The calculations for resonance frequency shifts of a polymer beam due to the best possible magnetic field (permanent magnets; h = 0mm, z_0 = 1.8mm; dB/dz = 143 T^2/m) are in Table 3.6.

While the frequency shifts for the polymer beam due to the magnetic field may be detectable since they do fall within the estimated uncertainty of 0.013Hz, the differences between frequency shifts do not. An uncertainty smaller than 0.009 Hz would be required to sense the differences in frequency shifts due to a 10% variance in magnetic susceptibility. Since the uncertainty of a polymer beam is expected to be larger than the evaluated silicon beam uncertainty, the differences will be undetectable.

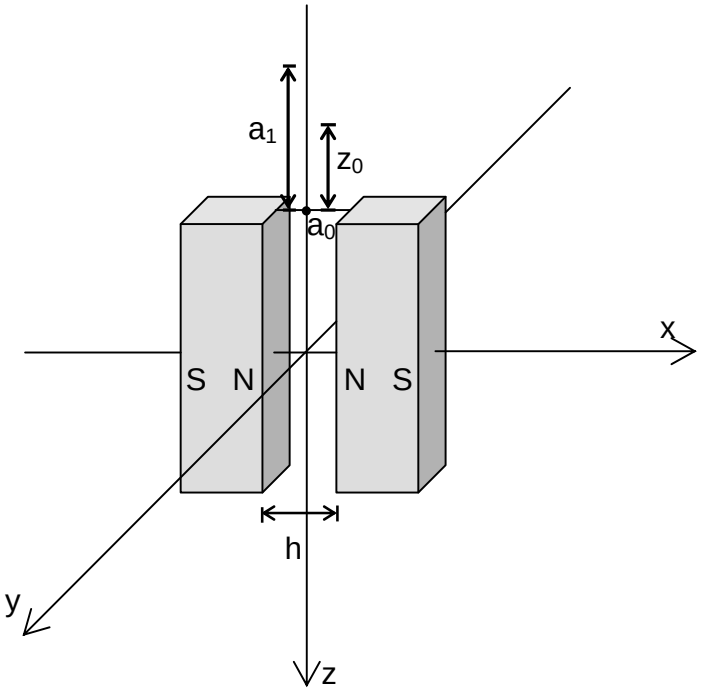

Figure 3.1 - Permanent magnet alignment
(beam dimensions and orientation shown in Figure 3.3)

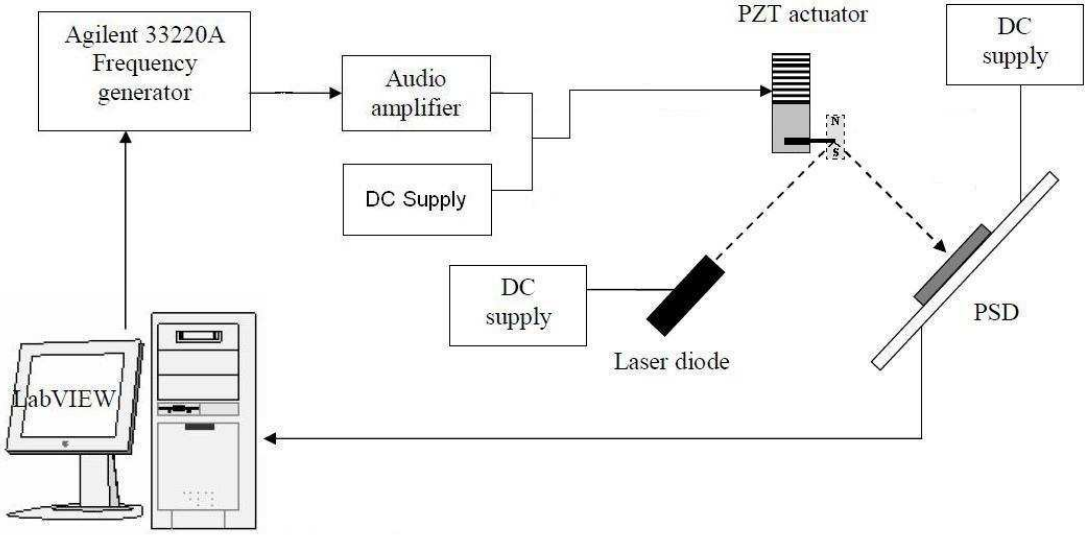

Figure 3.2 - Flow chart of the resonance frequency detection method

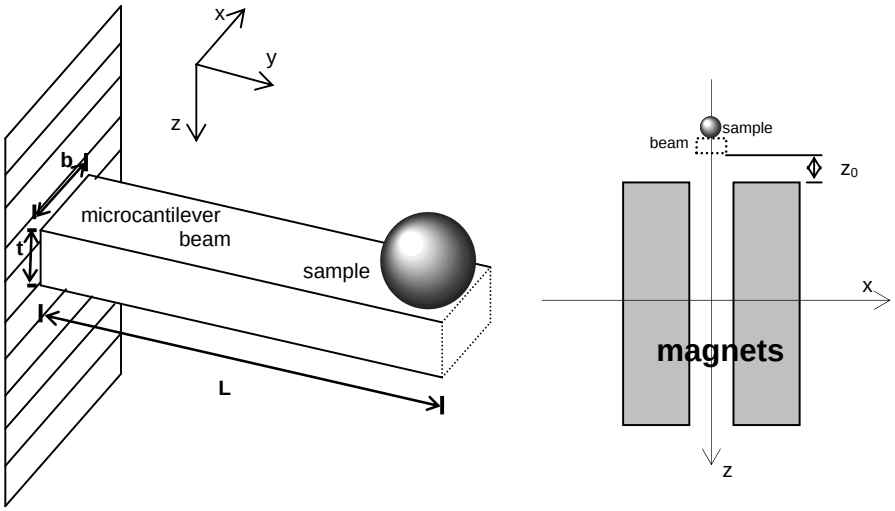

Figure 3.3 – Detailed diagram of the beam, sample, and force system

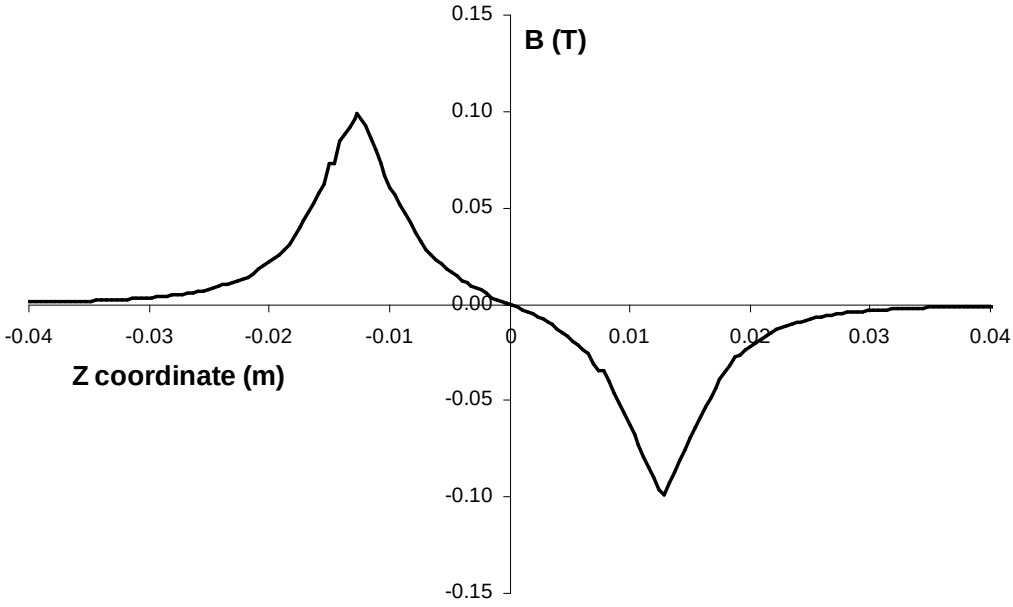

Figure 3.4 - Plot of the magnetic field in the z-direction along the z-axis for h=5mm and z_0 = 3.8 mm. The edges of the magnets are at z=± 0.0127.

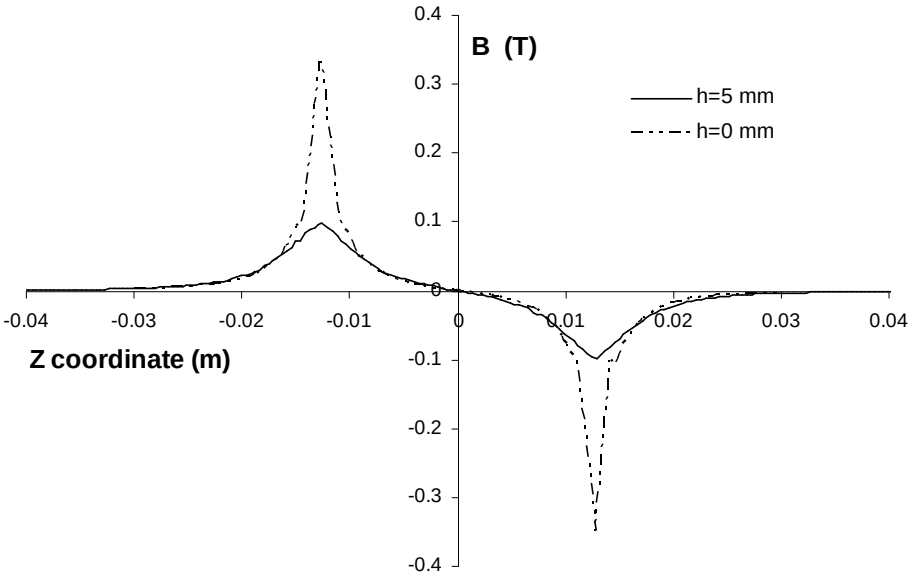

Figure 3.5 – Plot of the magnetic field distribution for *h*=0mm and *h*=5mm.

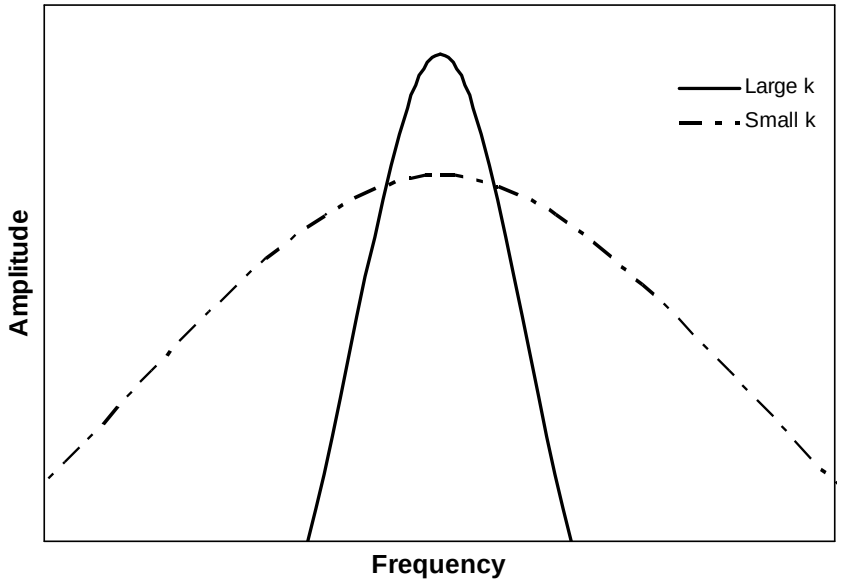

Figure 3.6 –Graphic example of the frequency sweep differences due to different *k* values

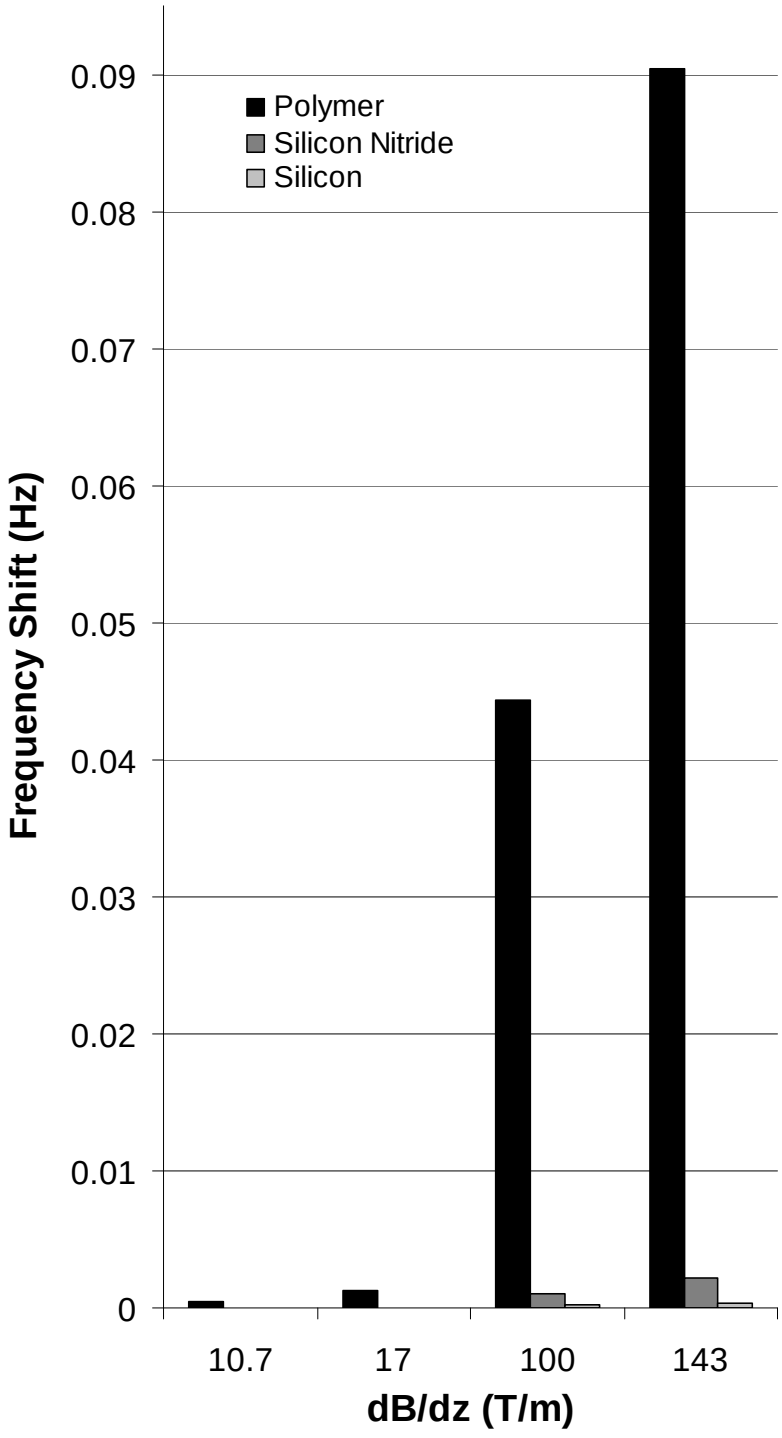

Figure 3.7 – Resonance frequency shifts of three beam types resulting from four different magnetic field sources

Table 3.1 –COMSOL modeling inputs.

Model Type	magnetostatic (no currents)
Magnet Inputs	
B at a_0 a_1 Library material	0.1 T 3.5 cm Soft iron without losses
Surrounding space inputs	
Boundary condition	zero potential at a surrounding sphere with a 5cm radius
Relative permeability (ratio to permeability of air)	1

Table 3.2 –Experimentally determined resonance frequencies and uncertainties for three test silicon beams

Silicon Beam	Resonance Frequency (Hz)	Uncertainty (Hz)	Percent Uncertainty
1	151.77	0.0039	0.0026
2	248.00	0.0240	0.0097
3	679.00	0.0096	0.0014
bismuth	155		
bismuth and magnetic field	155		

Table 3.3 - Properties of three different beam types and dimensions

Property	Material		
	polymer	silicon nitride	silicon
density, ρ (kg/m^3)	850	3.44E+03	2.33E+03
length, L (m)	2.00E-04	1.00E-03	3.00E-03
width, b (m)	1.00E-04	1.00E-04	1.00E-03
thickness, t (m)	1.00E-07	9.00E-07	5.00E-05
E (Pa)	1.40E+09	3.35E+11	1.50E+11
beam volume (m^3)	2.00E-15	9.00E-14	1.50E-10
I (m^4)	8.33E-27	6.08E-24	1.04E-17
stiffness, k (kg/sec^2)	4.38E-06	6.11E-03	1.74E+02
mass of beam, m_b (kg)	1.70E-12	3.10E-10	3.50E-07
resonance frequency (Hz)	5.26E+02	1.45E+03	7.30E+03
(kHz)	0.53	1.45	7.30

Table 3.4 – Number of organelles that fit on beam tips

subcellular organelle	polymer and silicon nitride	silicon
small mitochondria	5.0E+05	5.0E+08
large mitochondria	5.0E+02	5.0E+05
ribosomes	6.25E+10	6.25E+13
small nuclei	3.76E+02	3.76E+05
large nuclei	4.7E+01	4.70E+04

Table 3.5 –Predicted resonance frequency shifts (in Hz) due to different magnet fields and gradients

Beam Type	h = 5 mm z_0 = 3.8 mm B*dB/dz = 0.535 T^2/m	h = 0mm z_0 = 3.8 mm B*dB/dz = 0.918 T^2/m	h = 0 mm z_0 = 1.8 mm B*dB/dz = 11.44 T^2/m	superconducting magnet B*dB/dz = 1300 T^2/m
polymer	0.000507	0.001280	0.090400	0.044300
silicon nitride	0.000012	0.000030	0.002150	0.001050
silicon	0.000002	0.000006	0.000397	0.000194

Table 3.6 - Differences in frequency shifts as a result of 10% variance in magnetic susceptibility for a 143 T/m gradient for a polymer beam

magnetic susceptibility	polymer frequency shift (Hz)
same as water	0.09040
10% larger	0.09940
10% smaller	0.08140

4. Magnetophoresis

4.1 Background

Magnetophoresis is a technique that applies a magnetic field perpendicular to unidirectional laminar flow thereby causing a solution containing particles of different sizes and/or magnetic susceptibilities to displace with varying magnetic velocities. The electric counterpart, electrophoresis, operates under the same principles except an electric field is applied to particles that have an intrinsic charge or is 'tagged' with an electric charge. Electrophoresis is commonly used for the separation of different particles such as DNA, cells or polymer microspheres for use in medical and biological applications while magnetophoresis is being explored for similar purposes (Pamme et al., 2006; Karle et al., 2009; Iwasaka et al., 2001). The technique appears promising since it relies on intrinsic particle properties analogous to electrophoresis. While the benefits and effectiveness of magnetophoresis as a sorting tool are being studied, the potential of the technique to identify the magnetic susceptibility property has received very little consideration. If the magnetically produced velocities can be quantified, the magnetic susceptibility can be calculated.

In this study, an apparatus producing laminar flow through a long, narrow channel oriented vertically is considered (see Figure 4.1). A particle with magnetic susceptibility introduced into the channel will displace as it passes through a magnetic field. Since particles of interest and the magnetically produced displacements are micro- and nano-scale in size, the apparatus must be able to detect the velocities and calculate the

magnetic susceptibility with sufficient accuracy. As a result of the small scales, a number of unique challenges arise. The inability to measure the size and mass of very small particles presents a complication since the magnetic force depends on the mass of the particle (see Equation 2.1); a known mass is necessary to calculate the magnetic susceptibility. The particle size is also integral to the calculation of the magnetic susceptibility due to the Stokes drag force (illustrated in section 4.2, following). Pinpointing the location of the particle of interest at specific times (resulting in a velocity) visually or through some other sensing technique is also difficult. Potential sensing techniques include a high-quality CCD camera, fluorescent tagging, and laser light scattering. In addition, the sensitivity and accuracy capability of the technique to detect the magnetic susceptibility must be adequate to distinguish between different subcellular organelles (an estimated 10% variance in magnetic susceptibility). The following sections discuss the theory behind magnetophoresis and an experimental trial run to address many of the previously mentioned challenges.

4.2 Theory

A model of particle movement through the fluid can be used to calculate the magnetic susceptibility. The total velocity of a particle of interest can be separated into two perpendicular components: the velocity due to the magnetic field in the z_f-direction and the velocity due to the laminar flow in the x_f-direction

$$\vec{U}_{tot} = \vec{U}_{zf} + \vec{U}_{xf} . \tag{4.1}$$

This separation is applicable for laminar flow.

A free body diagram illustrating all of the forces acting on the particle is shown in Figure 4.2. The relative directions of the magnetic force F_{mag}, the opposing drag force F_D, and gravity F_g are indicated as well as the relationship to the flow axes, x_f and z_f. According to Newton's Second Law, the sum of the three force contributions in the z_f-direction is equal to zero since there is no acceleration

$$F_{mag}\cos\Phi - F_D\cos\Phi + F_g\sin\Phi = 0\,. \tag{4.2}$$

In an ideal situation, the gravitational force and the fluid flow would be parallel ($\Phi = 0$) resulting in no gravitational contribution to U_{zf}. However, even a small Φ can have a large impact so it must be considered.

The force on the particle due to the magnetic field is dependent on the magnetic susceptibility of the surrounding fluid $\overline{\chi}_{fl}$, the magnetic susceptibility of the particle of interest $\overline{\chi}_p$, and the volume of the particle V_p

$$F_{mag} = \frac{\left(\overline{\chi}_p - \overline{\chi}_{fl}\right)V_p B\dfrac{dB}{dz}}{\mu_0}\,. \tag{4.3}$$

Assuming the particle is diamagnetic, the magnetic force can be increased and thus easier to detect by using a paramagnetic solution for the fluid since $\overline{\chi}_{diamagnetic} < 0$ and $\overline{\chi}_{paramagnetic} > 0$.

Particle displacement due to the magnetic force produces an opposing drag force as a result of the surrounding fluid. When the Reynolds number based on the radius of the particle is much smaller than one ($Re_D << 1$), the viscous drag force on the particle is the Stokes drag force

$$F_D = 6\pi\eta r U_{zf} C_w \tag{4.4}$$

where η is the viscosity of the fluid, r is the radius of the particle, and C_w is the viscous drag coefficient.

The viscous drag coefficient C_w is due to the planar surfaces of the flow channel. As a result, C_w is dependent on the particle radius, the channel depth, and the location of the particle within the channel. Happel et al. (1973) published analytic formulas for C_w at three locations in a channel (see Figure 4.3). In the first configuration, the particle is located in the middle of the two walls resulting in the drag coefficient C_{w1}

$$C_{w1} = \left(1 - 2.008\frac{r}{a} + 3.344\frac{r^3}{a^3} + 3.36\frac{r^4}{a^4} - 5.408\frac{r^5}{a^5}\right)^{-1} \tag{4.5}$$

where r is the radius of the particle, a is the channel depth, and the particle is located at $y = 0$. In the second configuration the particle is located closer to one wall than the other resulting in the drag coefficient C_{w2}

$$C_{w2} = \left(1 - 1.3052\frac{r}{a} + 1.18\frac{r^3}{a^3} - 2.096\frac{r^4}{a^4} - 2.0608\frac{r^5}{a^5}\right)^{-1} \tag{4.6}$$

for a particle location of $y = a/6$. In the third configuration, the particle is far enough away from one wall and close enough to the other wall that only one wall creates the drag force on the particle, resulting in the drag coefficient C_{w3}

$$C_{w3} = \left(1 - \frac{9r}{16a_3} + \frac{r^3}{8a_3{}^3} - \frac{45r^4}{256a_3{}^4} - \frac{r^5}{16a_3{}^5}\right)^{-1} \tag{4.7}$$

where a_3 is the distance from the closest wall. In this study, a value for a_3 of $a/4$ (for $y = a/4$) will be used for evaluation purposes. Since all drag coefficient values are dependent on the ratio of particle radius to a characteristic length that is dependent on channel depth, the ratio of particle radius r to channel depth a (r/a) is an important design parameter that

affects the amount of drag. To avoid blockage, the *r*/*a* ratio should be less than 0.25 (Tarn et al., 2009).

In the ideal situation where $\Phi = 0$, $F_D = F_{mag}$ (in Equation 4.2) and the velocity due to the magnetic force is

$$U_{zf} = \frac{F_{mag}}{6\pi\eta r C_w} \quad . \tag{4.8}$$

Solving Equations 4.2 and 4.8 for $\overline{\chi}_p$ allows calculation of $\overline{\chi}_p$ from experimentally determined values of U_{zf}

$$\overline{\chi}_p = \frac{6\pi\mu_0\eta r C_w U_{zf}}{V_p B \frac{dB}{dz}} + \overline{\chi}_{fl} . \tag{4.9}$$

When $\Phi \neq 0$, then the magnetic susceptibility will include a gravitational term

$$\overline{\chi}_p = \frac{6\pi\mu_0\eta r C_w U_{zf} - mg\tan\Phi}{V_p B \frac{dB}{dz}} + \overline{\chi}_{fl} . \tag{4.10}$$

4.3 Method

To determine the feasibility of the magnetophoresis technique, it is necessary to implement an experimental magnetophoresis system to assess several key components. A study of the system will allow evaluation of desired unidirectional flow field production, a variety of flow velocities and channel depths, and sensitivity and accuracy of velocity detection methods. The following section details the experimental apparatus, fluid and particle samples, and the procedures executed to examine the key characteristics.

Apparatus

The apparatus is comprised of a flow channel and a mounting device. The channel is constructed with an inlet, outlet and an additional inlet which allows introduction of test particles. The mounting device facilitates illumination, recording of the particle movement, and placement in the superconducting magnet bore.

The basic flow channel structure is designed to gradually spread fluid from the inlets into a channel and then condense into the outlet. To assure laminar flow, the channel length l in the flow direction is much larger than the width w and thickness a ($l>>w, a; w>>a$). The design was created to be cost and labor efficient, while allowing visual confirmation of the particle movement. The channel is constructed using three layers, shown in Figure 4.4. The outer dimensions of all three pieces are approximately 5.1 cm by 16.0 cm. The two outer layers, referred to as cover slips, are made of glass with thickness 2.27 mm. The top piece has three holes cut in it to allow the fluid to flow in and out of the channel. The larger holes have a diameter of 0.635 cm (inlet 1 and outlet 2), while the smaller hole has a diameter of 0.3175 cm (inlet 2, as labeled in Figure 4.4). The middle layer is silicon gasket with a 3 cm by 9 cm channel cut in the mid-section. Two different channel depths were studied corresponding to silicon gasket thicknesses of 1.18 mm and 0.254 mm. Three fluid fittings were glued over the holes to allow attachment of tubes for the fluid flow. The three layer channel constructed with the thicker silicon gasket was clamped using machined ‘H’ clamps (see Figure 4.5a). The channel with the thinner silicon gasket was clamped using ‘tarp clamps’ (see Figure 4.5b).

The flow channel, lighting and visualization components are mounted onto a machined piece of plastic to allow the apparatus to slide in and out of the bore of a 5T superconducting magnet (Center for Interdisciplinary Applications in Magnetic Resonance) while maintaining a stable physical relationship between the components (see Figure 4.6). The plastic was machined in a circular shape to have an outer radius of 70 cm to fit precisely within the bore interior of the same radius. Portions on the sides were cut-off to allow a piece of PVC pipe to be screwed on to serve as a handle. Slots were cut into the plastic to mount the lighting, flow channel, and camera as shown in Figure 4.7. Two LEDs (CCS America, Inc, LDL-34x8-SW; 67mW, λ = 400-700 nm) are mounted above and below at an angle to illuminate the area of interest (see Figure 4.6). The microscope lens (7.5mm Elmo lens, 1:1.6, code 9250) and camera (Elmo MN-42, magnetic field tolerant) are mounted to capture the area of interest. A prism is attached to the camera to rotate the image appropriately (see Figure 4.8). The apparatus is designed so that, when placed in the magnet, the flow channel is oriented as shown in Figure 4.9. The z-axis of the cylindrical magnet is aligned with the z_f-axis of the flow channel so that the magnetic displacement occurs in the z-direction. The x_f-axis of the flow channel is aligned vertically and parallel to gravity. While the apparatus is designed to provide this ideal orientation, it is not completely stable. As a result, it is possible that there is some offset angle Φ between the x-z and x_f-z_f coordinate systems (Figure 4.2).

The magnetic field in the z-direction and magnetic field gradient with respect to the z-axis for a central radial location are in Figure 4.10 and 4.11 respectively where z = 0 cm at the center of the bore as shown in Figure 4.8. The magnetic field varies from 0T to 5T and the gradient varies from 0 T/m to -11.065 T/m. The magnetic field and gradient

product with respect to the z-coordinate is presented in Figure 4.9. The figure clearly shows that the maximum product of -38.91 T^2/m occurs at z = 50 cm. To maximize the particle displacement, the flow channel will be centered at the maximum location.

Fluid and Particle Samples

Experimental tests were run using diamagnetic polystyrene test particles and a paramagnetic solution consisting of water and manganese chloride tetrahydrate ($MnCl_2$). An aqueous suspension of diamagnetic polystyrene particles of diameter 101.63 ± 0.17 μm was obtained from Polysciences, Inc. According to two separate sources, polystyrene has magnetic susceptibility $\overline{\chi}_1$ = -8.21x10^{-6} (Tarn et al., 2009) or $\overline{\chi}_2$ = -1.02x10^{-5} (Tanimoto et al., 2005). Paramagnetic solutions of 9.76% manganese chloride by weight were prepared by dissolving manganese chloride tetrahydrate (Fisher Scientific) in RO water. The solution was filtered through VWR International filter paper to remove any dust or undissolved $MnCl_2$ particles. The solution has the following characteristics: η = 1.10x10^{-3} kgm^{-1}sec^{-1} at 20˚C (Phang, 1980) and $\overline{\chi}_{fl}$ = 1.30x10^{-5}. The magnetic susceptibility of the fluid was calculated using Equation 4.11

$$\overline{\chi}_{fl} = \sum_{k=1}^{n} p_k \overline{\chi}_k \tag{4.11}$$

where $\overline{\chi}_{fl}$ is the magnetic susceptibility of the solution, $\overline{\chi}_k$ is the magnetic susceptibility of the components and p_k is the weight fraction of the respective components (Karolik et al., 1979). The solution is composed of two components, water and $MnCl_2$, with weight fractions of 0.9024 and 0.0976 and dimensionless magnetic susceptibilities of -7.01x10^{-7} and 1.4x10^{-4}, respectively.

Procedure

Figure 4.13 details the schematic of the experimental set-up. The flow into inlet 1 is driven by a programmable syringe pump (New Era Pump Systems, model # NE-1000). Paramagnetic fluid ($MnCl_2$ and H_20) containing the test particles is slowly injected from a syringe by hand through inlet 2. After moving through the channel, the fluid exits through the outlet to an outlet reservoir. A LabVIEW program drives the data collection by the camera. The program collects, displays, and imports JPG images to a designated folder every 0.5 seconds.

A sequence of images that contains the movement of a particle is opened in ImageJ (National Institute of Health freeware) and the contrast is increased if necessary. The particle is manually tracked through each frame by placing the cursor on the particle and clicking (see Figure 4.14 and 4.15). The pixel locations are recorded and then the x_c and z_c positions are plotted against time in Excel. Trendlines are fit to the data so that the slopes give the x_c and z_c velocity components. The data for any particle are considered an outlier if the coefficient of determination, R^2, is less than 0.8. To ensure that the z_c velocities are the magnetic velocities, any angular offset between the x_f-z_f (aligned with flow) and the x_c-z_c (aligned with the camera image) coordinate systems must be resolved. Particle movement is tracked outside of the magnet to establish the x_c-z_c coordinate system, giving the magnitude of the velocity vector $\vec{U}_{f0}$ and the angle between the velocity vector and the x_c-axis θ_0 (see Figure 4.16). The x_f and z_f velocity components of particles inside the magnet bore are used to find the magnitudes of the velocity vectors

$\vec{U}_c$ and the angular offset with respect to the x_c axis θ_m. Using θ_m, θ_0, and $\vec{U}_c$, the x_f and x_z velocity components (U_{xf} and U_{zf}) are calculated with Equations 4.12 and 4.13

$$U_{zf} = U_c \sin(\theta_m - \theta_0) \tag{4.12}$$

$$U_{xf} = U_c \cos(\theta_m - \theta_0). \tag{4.13}$$

The entire data collection and processing is summarized in flow chart format in Figure 4.17.

All of the previous calculations involved velocities with units of pixels per second. To obtain the desired units of mm/sec, the number of pixels per millimeter was measured. A clear ruler was taped onto the channel on the side closest to the camera. An image is collected. In ImageJ, a line is drawn over multiple millimeters. The length of the line in pixels is evaluated against the length of the line according to the ruler to find the number of pixels per millimeter. The process is repeated with the ruler taped to the back and the two values are averaged to find the final pixels/mm scaling.

In addition, the particles are separated into three regions: (1) particles located at least one third of the channel width away from the walls $y > a/3$, (2) those that are located at least one fourth of the channel width away $a/3 > y > a/4$, and (3) those that are even closer to the wall $y < a/4$ (See Figure 4.18). For particles in the first region, an average of C_{w1} and C_{w2} ($\overline{C}_{w12}$) is used for the viscous drag coefficient to calculate the magnetic susceptibility while an average of C_{w2} and C_{w3} ($\overline{C}_{w23}$) is used for particles in the second region. When calculated for the thick channel dimensions, $\overline{C}_{w12}$ is 1.0924 and $\overline{C}_{w23}$ is 1.0985. For the thin channel dimensions $\overline{C}_{w12}$ is 1.5985 and $\overline{C}_{w23}$ is 1.7577. All particles located in the third region will be eliminated from consideration when

calculating magnetic susceptibilities. The particles are separated to decrease the U_{zf} uncertainty by predicting the location of the particle in the channel and getting a more accurate value for the drag coefficient. The correct particle separation can be identified using the equation for the flow velocity U_{xf} through a channel as a function of y (see Figure 4.18 for axial orientation)

$$U_{xf}(y) = \frac{1}{2\eta}\frac{\Delta p}{l}\left[\left(\frac{a}{2}\right)^2 - y^2\right] \tag{4.14}$$

where $y = 0$ along the center of the channel, Δp is the pressure gradient, and l is the length of the channel. Since the maximum flow velocity U_{xmax} occurs along the center of the channel ($y = 0$), the ratio of U_{xmax} to the flow velocity for a particle located one third of the channel width away from the wall U_{xt} ($y = a/6$) is utilized to simplify Equation 4.14

$$\frac{U_{xt}}{U_{x\max}} = \frac{\left[\left(\frac{a}{2}\right)^2 - \left(\frac{a}{6}\right)^2\right]}{\left(\frac{a}{2}\right)^2} = \frac{8}{9} \tag{4.15}$$

U_{xmax} is unknown, however the relationship between U_{xmax} and U_{avg} is known ($U_{xmax} = 3/2U_{avg}$) the ratio of U_{xt} to U_{avg} is 1.33. When the above process is repeated for a particle that is a distance of $a/4$ from the channel wall ($y = a/4$), the ratio of U_{xt} to U_{avg} is 0.75. When calculating a magnetic susceptibility value from the magnetic velcocity, all particles with a ratio of flow velocity to average flow velocity greater than 1.33 use $\overline{C}_{w12}$ as the drag coefficient while those with a ratio less than 1.33 and greater than 0.75 use $\overline{C}_{w23}$.

The goal of the magnetophoresis study is to evaluate desired unidirectional flow field production, a variety of flow velocities and channel depths, and sensitivity and accuracy of velocity detection methods. The evaluations will be completed as follows:

The flow through the channel design is examined using ANSYS-CFX. In particular, the study allowed confirmation that the fluid flow is laminar over the majority of the channel. The flow field data is also used to place the microscope camera in the optimum location.

Data is collected for two different flow velocities through the 1.18mm thick channel (r/a = 0.043) and at another speed through the 0.254mm thick channel (r/a = 0.199) to allow velocity and channel depth analysis. The data are compared to maximize the probability that a given particle will move at the faster rate with a goal of amplifying U_{zf}. The particles moving at a slower pace will be closer to a wall and should have a smaller magnetic velocity since the drag force will be greater (when the fluid is pumped at a steady and uniform rate). The uncertainties of the data will be compared to determine the effect of channel depth and velocity.

The accuracy of the visually detected and calculated U_{zf} will be determined by picking 5 random particles of different visibility qualities and repeating the manual tracking process 10 times per particle. The results will be averaged and the uncertainty U will be found by calculating the standard deviation σ (where $U = 2\sigma$). When resolving differences between the x_c-z_c and x_f-z_f coordinate systems, the uncertainty in determining the angles contributes further to the uncertainty of U_{zf}. Multiple particles are tracked outside of the magnet bore and averaged to determine θ_0. Twice the standard deviation of the particle angles is the uncertainty (see Appendix B for a full error analysis).

4.4 Results

The results of the flow characterization and experimental trial runs are discussed in detail in the following sections.

Flow Characterization

To confirm that the flow through channels of the given dimensions ($l>>w$, a; $w>>a$) is laminar, the Reynolds number is calculated using Equation 4.16

$$\mathrm{Re} = \frac{U_{avg} a}{\eta}. \tag{4.16}$$

where U_{avg} is the average particle flow velocity calculated from all particles with the same syringe pump rate. For the thicker channel, the depth is 1.18 mm and the average flow velocities are 0.63 and 1.09 mm/sec so the Reynolds numbers are 6.76×10^{-4} and 1.17×10^{-3}. For the thinner channel, the depth is 0.254 mm and the flow velocity is 1.44 mm/sec resulting in a Reynolds number of 3.33×10^{-4}. Both Reynolds numbers are well below the laminar threshold of 2300.

The Reynolds number where the characteristic length is the diameter of the particle ($Re = U_{avg} d/\eta$) must be much smaller than one to enable the use of the Stokes drag force in Equation 4.4. The velocity of flow through the thick and thin channel result in Reynolds numbers of 1.08×10^{-4} and 2.33×10^{-5}, both of which are much smaller than one.

The effect of inlet 2 (see Figure 4.6) on the flow field was examined to confirm that the flow through the area of focus is laminar so that any displacement in the z-

direction is only due to the magnetic force. The modeling capabilities of ANSYS-CFX are used to model the flow of water through a channel of similar shape for a range of input values and dimensions. Inlet velocities were varied from 0.5 to 2 mm/sec and the channel depth varied from 0.5 mm to 1.5 mm. The channel dimensions are the same as those presented in Section 4.3 and Figure 4.4, except the channel length is shortened to 6 cm. Representative ANSYS-CFX modeling results are shown as images of the streamlines (Figure 4.19) and the cross-section of the flow field a short distance following inlet 2 (Figure 4.20). Both images clearly illustrate the desired 2-Dimensional laminar flow field.

Trial Run

All data collected and presented in Figures 4.21-4.28 were processed to account for misalignment between the camera and flow coordinate systems, but not gravity. The experimentally determined magnetic velocity U_{zf} values of each particle in the channels with depths of 1.18 mm and 0.254 mm are shown in Figures 4.21 and 4.22, respectively. The magnetic velocity is plotted against the particle flow velocity U_{xf}. Both velocities are shown as a ratio to the average particle velocity calculated from all particle flow velocities of the same syringe pump rate. In addition, the cut-off lines of 0.75 and 1.33 are shown. Four particles for the thick channel and three particles for the thin channel are located in region 3 resulting in elimination from consideration. Two particles for the thick channel and one particle for the thin channel are located above the cut-off ratio of 1.33 in region 1 leaving the rest of the particles in region 2. In Figures 4.23 and 4.24, the magnetic velocities were used to generate distance vs. time plots of the particle

trajectories to allow comparison. Additionally, the expected magnetic velocity trajectories (labeled in each figure) are included for all possible combinations of C_w and magnetic susceptibility values. Figures 4.25 and 4.26 plot the magnetic velocity values for each particle and indicate the expected velocities calculated using Equations 4.4 and 4.8.

Experimental magnetic susceptibility values are calculated for each particle using Equation 4.9. Table 4.1 details all of the relevant inputs where $\overline{C}_{w12}$ is the average of C_{w1} and C_{w2}, $\overline{C}_{w23}$ is the average of C_{w2} and C_{w3}, and the subscripts *A* and *B* indicate the thick and thin channel respectively.

The experimental magnetic susceptibilities of the particles for the thick and thin channel are plotted in Figures 4.27 and 4.28 respectively. Error bars are included for each particle (see Appendix B for error calculation). The two published magnetic susceptibility values for polystyrene are plotted for comparison.

In addition, data were gathered at four other locations within the bore (z = 10, 20, 30 and 40 cm) for the paramagnetic solution and at all 5 locations using a water solution. The processed data are presented in Appendix C.

4.5 Analysis and Discussion

The following section analyzes the significance of the flow field and trial run results as well as the implications on the feasibility of magnetophoresis to identify the magnetic susceptibility of subcellular organelles.

Flow Characterization

The flow characterization results in Section 4.4 confirm expectations that the channel design produces the desired flow field. In addition, the Reynolds numbers indicate that the syringe pump speeds used in the trial runs are well within the limitations.

Trial Run

The trial run offers several valuable insights to this particular magnetophoresis application concerning channel depth, flow velocity, calculated magnetic susceptibility consistency and accuracy, and error minimization.

The effect of channel depth (and r/a ratio) on particle velocities is best illustrated by Figures 4.21 and 4.22. The figures confirm the tendency of particles to have a velocity closer to the average fluid velocity for a thinner channel depth and larger r/a ratio. There are fewer particles below the 0.75 cut-off velocity ratio for the channel with a depth of 0.254mm and r/a ratio of 0.199 than for the channel with a depth of 1.18mm and r/a ratio of 0.043and the spread and variation of the flow velocities is largest for the thicker channel. These conclusions are important because particles with a velocity close to the average velocity are further from the channel walls than slower particles. As a result, there is less drag resistance thereby maximizing the magnetic velocity and ease of detection. In addition, less variation in flow velocities leads to consistency in measurements and calculations of magnetic susceptibility. However, the error bars of individual particle magnetic velocities and susceptibilities are significantly smaller on average for the thick channel data than for the thin channel data (Figures 4.25-4.28), but that can be explained by flow velocity differences.

The effect of flow velocity on particle velocities and calculated magnetic susceptibilities is identified by examining Figures 4.21, 4.25 and 4.27. As in the channel depth analysis, Figure 4.21 demonstrates that a faster flow velocity decreases the variation in particle flow velocities. The collection of data at two different speeds for the same channel depth shows no significant differences in magnetic velocity or magnetic susceptibility magnitudes in Figures 4.25 and 4.27. As a result, an optimal syringe pump rate can be chosen for other reasons, such as visualization purposes or to minimize uncertainty. Since the error bars in Figures 4.25 and 4.27 are significantly smaller for the particles with an average flow velocity of 0.63 mm/sec than for the particles with a faster average flow velocity of 1.09 mm/sec, a slower speed minimizes uncertainty. The average magnetic susceptibility uncertainties for flow velocities of 0.63 and 1.09 mm/sec are 1.06×10^{-6} and 1.67×10^{-6}. This is demonstrated further by examination of the 1.18 mm channel depth data in Figures 4.26 and 4.28, where an average magnetic susceptibility uncertainty of 1.20×10^{-5} occurs for a flow velocity of 1.44 mm/sec. The uncertainty magnitudes increase as the average flow velocity increases, regardless of channel depth.

As shown in the error analysis completed in Appendix B, the individual contributions to the total magnetic susceptibility can be analyzed to determine which has the greatest effect and should be targeted for improvement. The contribution of the magnetic velocity measurement error to the calculated magnetic susceptibility error is greatest. In fact, the other error contributions are relatively insignificant. See Table 4.2 for the breakdown of the error contributions for one particular particle as a representative error analysis (note that the total magnetic susceptibility error is the square root of the

sum of the components – see Equation B.2). As discussed previously, the uncertainty can be significantly decreased by decreasing the flow velocity.

While the uncertainty of magnetic susceptibility calculated from individual particles is an important factor, the consistency of all the calculated magnetic susceptibilities is just as essential. Figures 4.27 and 4.28 demonstrate that the calculated magnetic susceptibilities are less varied for the data gathered from the channel with a = 0.254mm and r/a = 0.199. For the thinner channel, the average magnetic susceptibility is 1.20×10^{-5} with a standard deviation of 2.35×10^{-6}. In contrast, the average magnetic susceptibility for the thick channel (r/a = 0.043) data is 8.88×10^{-6} with a standard deviation of 5.09×10^{-6}, which is more than twice as large as the value for the thin channel.

The consistency of the calculated magnetic susceptibilities is not nearly as crucial as the accuracy. Figures 4.23 – 4.26 provide easy comparison of the measured magnetic velocities to the expected magnetic velocities, while Figures 4.27 and 4.28 provide comparison of the experimental magnetic susceptibilities to the accepted values. An effect due to the superconducting magnetic field is detected but not to the degree that was theorized. The experimental values are significantly different than the expected and accepted values. The averages of the magnetic susceptibilities for the thick and thin channel particles are $+8.876 \times 10^{-6}$ and $+1.198 \times 10^{-5}$ respectively, compared to published values of -8.21×10^{-6} and -1.02×10^{-5}. The disparity can be explained by misalignment between the direction of flow in the channel and gravity ($\Phi \neq 0$). The average magnetic velocity for each channel and the accepted magnetic susceptibilities is used to find a theoretical Φ by solving Equation 4.10 for Φ

$$\tan\Phi = \frac{6\pi\mu_0\eta r C_w U_{zf} - \left(\bar{\chi}_p - \bar{\chi}_{fl}\right)V_p B\frac{dB}{dz}}{\mu_0 mg} \tag{4.17}$$

where the mass of the particle m is estimated using the given dimensions of a particle and the density of polystyrene 1050 m^3/kg (m = 5.77x10^{-10} kg). Angle measurements for Φ were not made and so must be calculated after the fact. Values for Φ are calculated for all combinations of drag coefficients and published magnetic susceptibility values and detailed in Tables 4.3 and 4.4. The average values of Φ are 4.53 (a = 1.18 mm) and 4.00 (a = 0.254 mm) degrees.

Subcellular Organelle Feasibility

The preceding analysis allows for feasibility evaluation of magnetophoresis to measure the magnetic susceptibility of subcellular organelles. This paper theorizes that magnetic susceptibility variance between types of subcellular organelles is approximately 10%. The capability of magnetophoresis to detect these differences can be examined in two ways: (1) analysis of the experimental magnetic susceptibility uncertainty and (2) investigation of magnetic velocity detection limitations.

The uncertainty of the magnetic susceptibility calculation must be less than 10% to allow for detection of the expected variances among organelle types. In this experimental study with polystyrene beads, flow velocities of 0.63, 1.09, and 1.44 mm/sec correspond to average magnetic susceptibilities of 8.63 ± 1.06x10^{-6}, 9.10 ± 1.67x10^{-6}, and 1.20 ± 26.8x10^{-5} respectively. The resulting uncertainty percentages are 12.3, 18.3, and 22.4% all of which fall outside the requirements.

The capability of magnetophoresis to detect a magnetic velocity is limited by the camera field of view and size of pixels. The field of view of the camera only allows for visual capture of particle movement within an approximately 2 x 2 cm box. As such, for any given flow velocity the particle only has 2 cm over which to displace due to the magnetic field. This could render small magnetic velocities virtually undetectable. In addition, the size of a particle or magnitude of magnetic velocity relative to a pixel must be large enough to enable particle and velocity detection. These concepts are useful in discovering the minimum detectable magnetic velocity. Since the pixel to millimeter conversion is 32.68 pixels/mm and the channel is approximately 20 mm long, at the slowest experimental flow velocity of 0.63 mm/sec the particle will take 31.75 sec to move through the image frame. Since the 100μm diameter particles are barely visually detectable, 100 μm displacement is used as the lower limit of detectability. 100μm corresponds to 3.27 pixels. Since the smallest detectable displacement is 3.27 pixels and the particle travels through the image in 31.75 sec, the minimum detectable magnetic velocity is 0.00316mm/sec or 3.16μm/sec. The average magnetic velocity uncertainty for the particles moving at an average flow velocity of 0.63 mm/sec (best case scenario), is 0.015mm/sec, resulting in a magnetic velocity lower limit of 0.00316 ± 0.015 mm/sec.

The magnetic velocity limitations are compared to the anticipated magnetic velocities to further evaluate technique feasibility. Table 4.5 details the anticipated magnetic velocities for each subcellular organelle type with the same magnetic susceptibility as water (-9.05×10^{-6}), in the 5T superconducting magnet, a channel depth of 0.254mm, an angle Φ value of zero, drag coefficient C_{w1}, and the same paramagnetic solution used in the trial run. The magnetic velocities vary from 1.37×10^{-8} mm/sec

(ribosome) to 0.016 mm/sec (large nucleus). For the current velocity detection method, only the small nucleus, large nucleus, and large mitochondria have magnetic velocities above the lower limit. The benefits of decreasing the channel thickness to 55μm and using a 17T superconducting magnet are explored in Table 4.6, where all other parameters remain the same. The *r*/*a* ratios vary from essentially zero to 0.2. The channel depth decrease does not produce a significant change in magnetic velocity magnitude; however, the benefits of a thinner channel depth discussed previously would still apply. When the magnetic field and gradient product is increased from -38.91 T^2/m to -1300T^2/m, the magnetic velocities vary from 4.57x10^{-7} mm/sec (ribosome) to 0.345 mm/sec (large nucleus). Once again, the magnetic velocities of the small nucleus, large nucleus, and large mitochondria are larger than the lower limit but now the small mitochondria are detectable by the current apparatus as well. In addition, since the organelle sizes listed are only exemplary the -1300 T^2/m magnetic field would enable detection of magnetic velocities for much smaller subcellular organelles than the -38.91 T^2/m magnetic field option allows. The significant increases in magnetic velocities would also make detection easier and more accurate.

The previous analysis is useful in looking at the technique capability to detect differences in magnetic velocities between different organelle types. The capability of magnetophoresis to detect the differences can be examined in two ways: (1) comparison of two different types of organelles that are different sizes (but similar) and magnetic susceptibilities and (2) comparison of two different types of organelles that are the same size with magnetic susceptibilities that differ by 10%. These scenarios are worst case; it is unlikely that two different subcellular organelles of interest will be the same size with

different magnetic susceptibility or of very similar size with the same magnetic susceptibility. Using the experimental system parameters for Table 4.6 described above and the larger magnetic field (17T magnet), these two options are explored in Table 4.7. The first option where the particles are similar in size with the same magnetic susceptibility produces a magnetic velocity difference of 0.0173 mm/sec and the second option produces a difference of 0.0046 mm/sec. Figure 4.29 plots the calculated magnetic velocities with uncertainties of 0.015mm/sec error bars for visual comparison. Since average flow velocities of 0.63, 1.09, and 1.44 mm/sec correlate to average magnetic velocity uncertainties of 0.015, 0.024, and 0.025 mm/sec, the differences for both options are undetectable for the current apparatus. However, it is likely that the first option difference would be detectable with apparatus modifications to improve uncertainty.

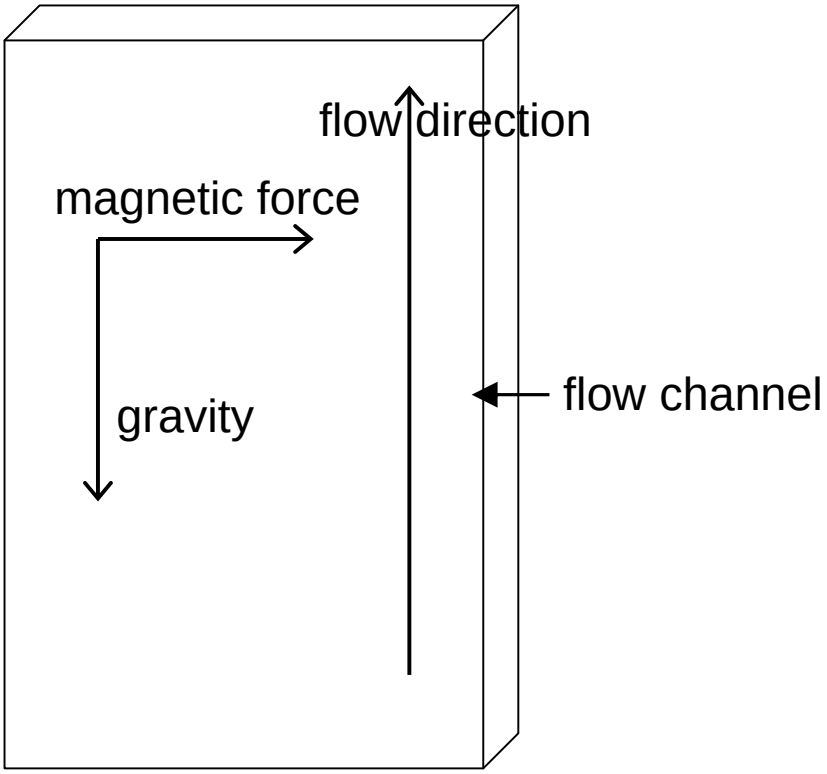

Figure 4.1 – A general pictoral depiction of the magnetophoresis technique implemented through a simple flow channel oriented vertically (parallel to gravity) and perpendicular to the magnetic force.

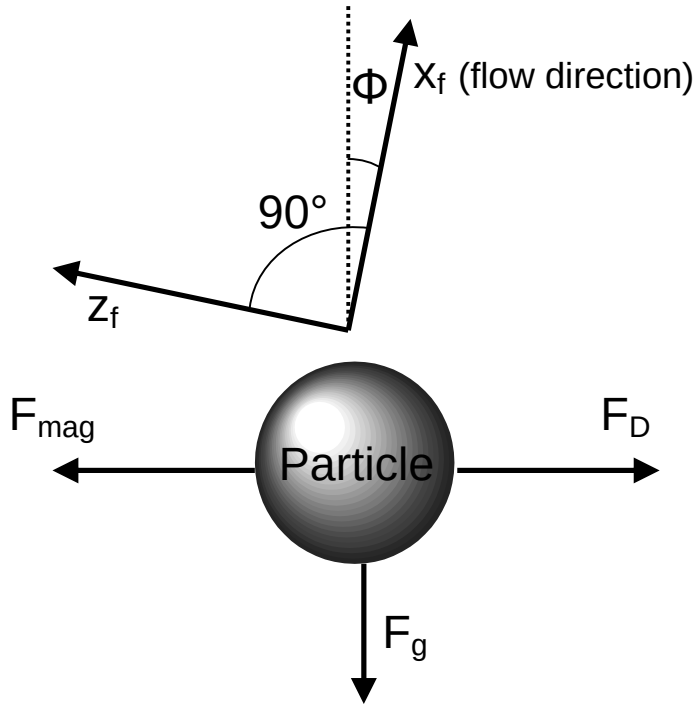

Figure 4.2 – Free body diagram of the particle forces

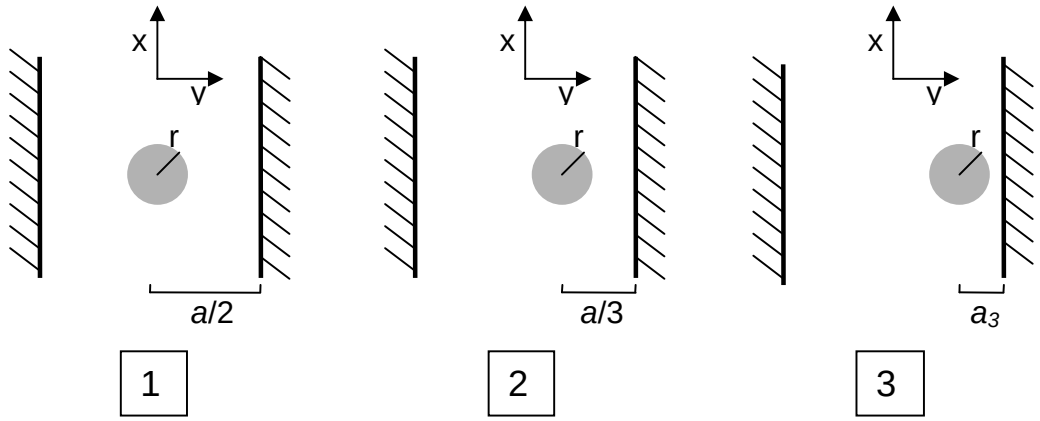

Figure 4.3 – Pictorial depictions of the three different particle locations for which C_w is known

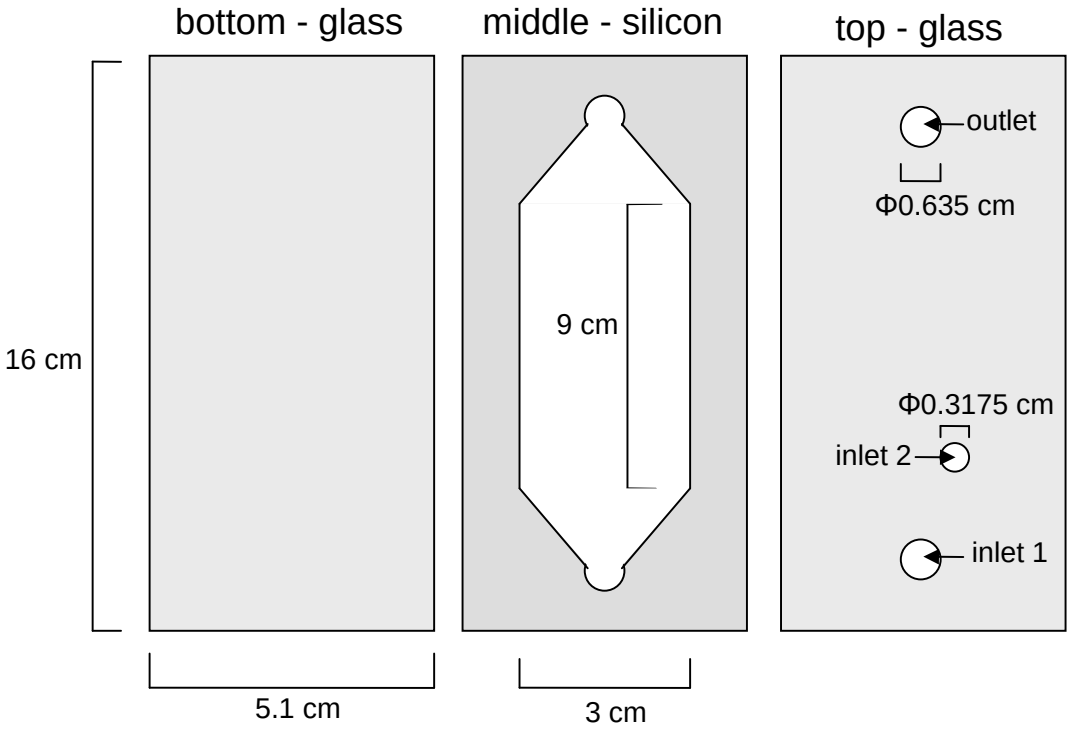

Figure 4.4 – Three piece flow channel design

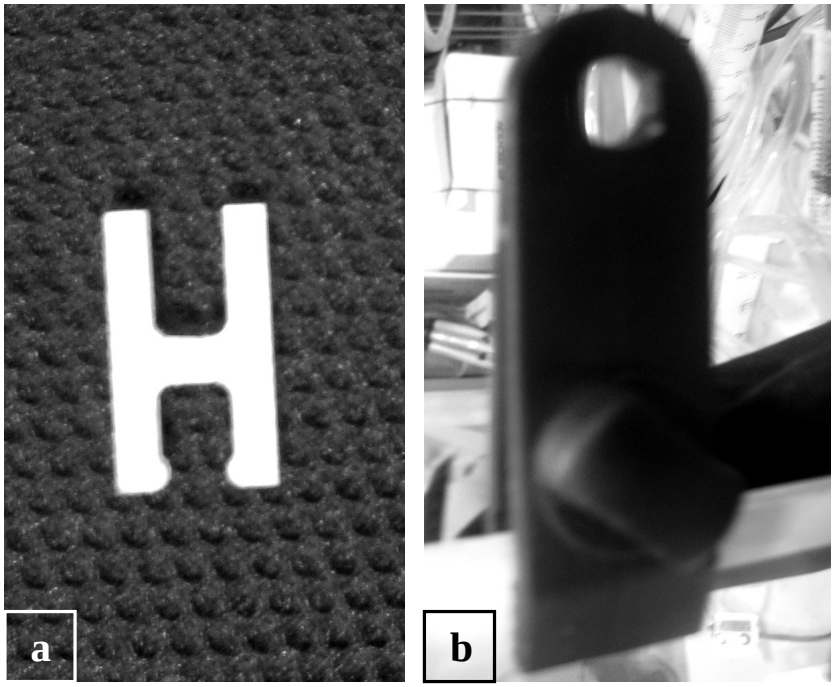

Figure 4.5 – a) Machined plastic 'H' clip
b) Plastic tarp clip

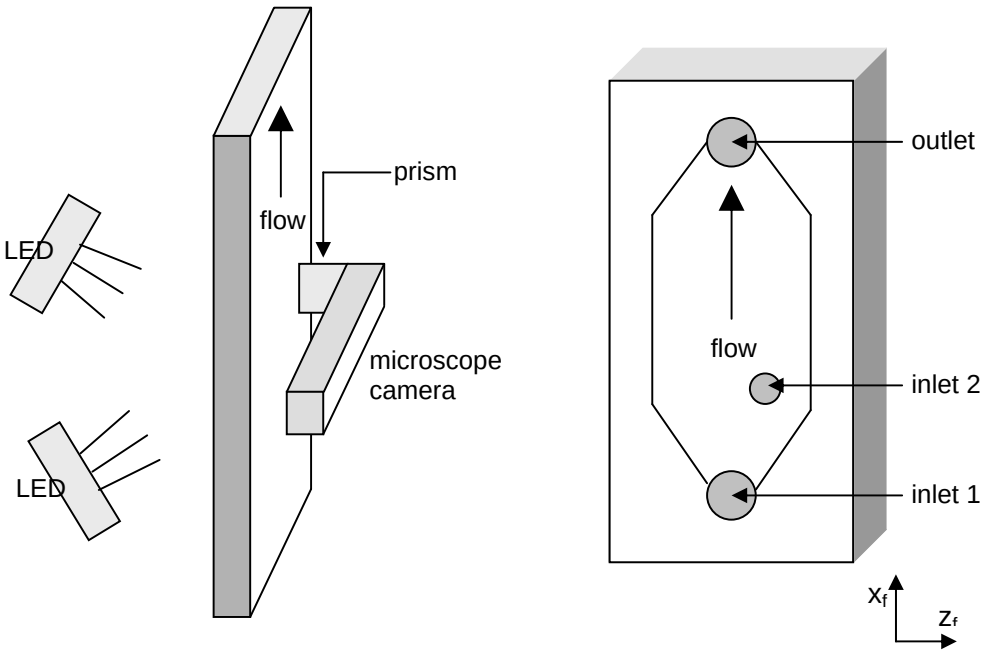

Figure 4.6 – Flow channel axial and spatial orientation

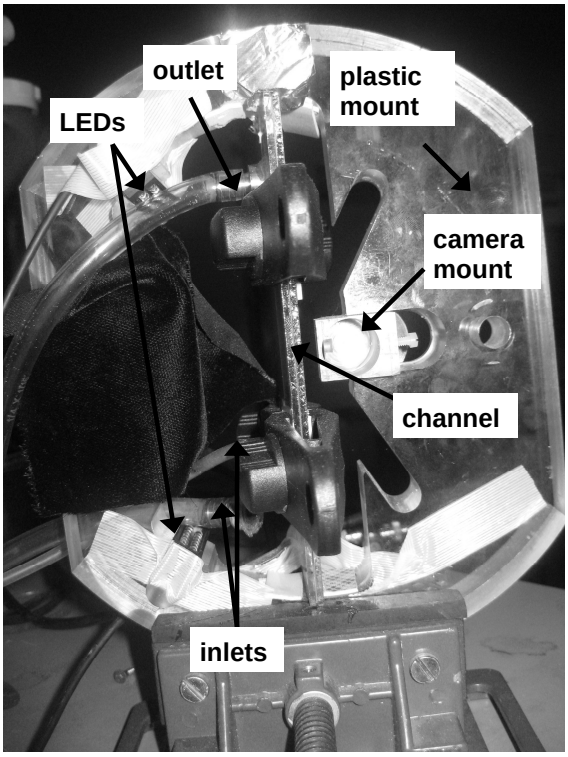

Figure 4.7 – Image of the plastic mount system

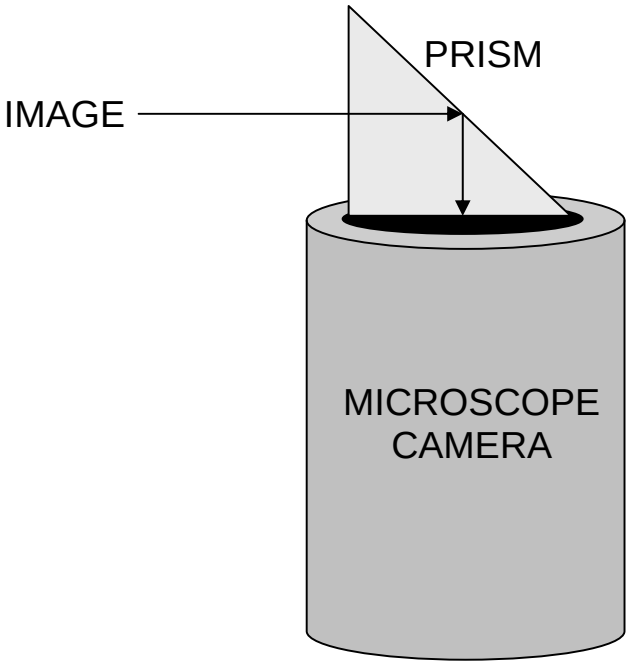

Figure 4.8 – Image reflection path through prism to camera lens

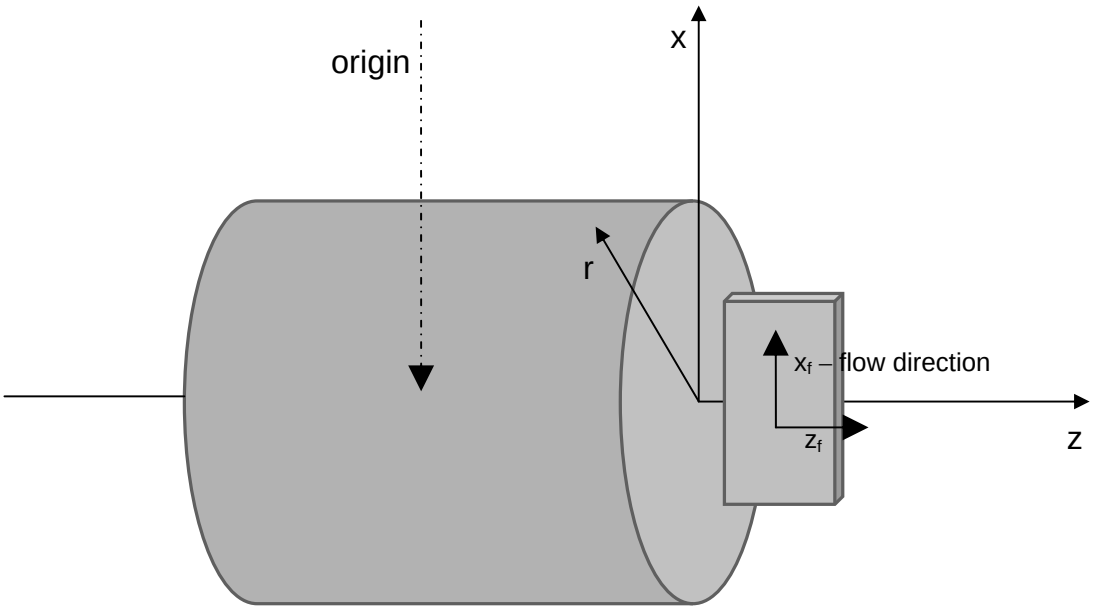

Figure 4.9 - Flow channel orientation with respect to the magnet bore

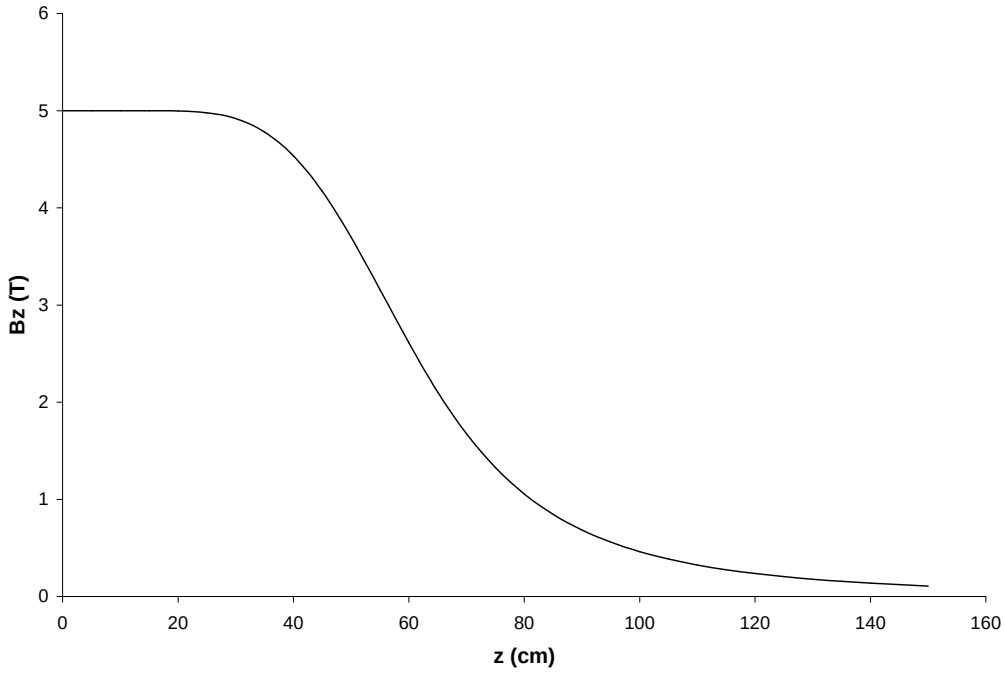

Figure 4.10 – Magnetic field (T) in the z-direction along the z-axis (cm)

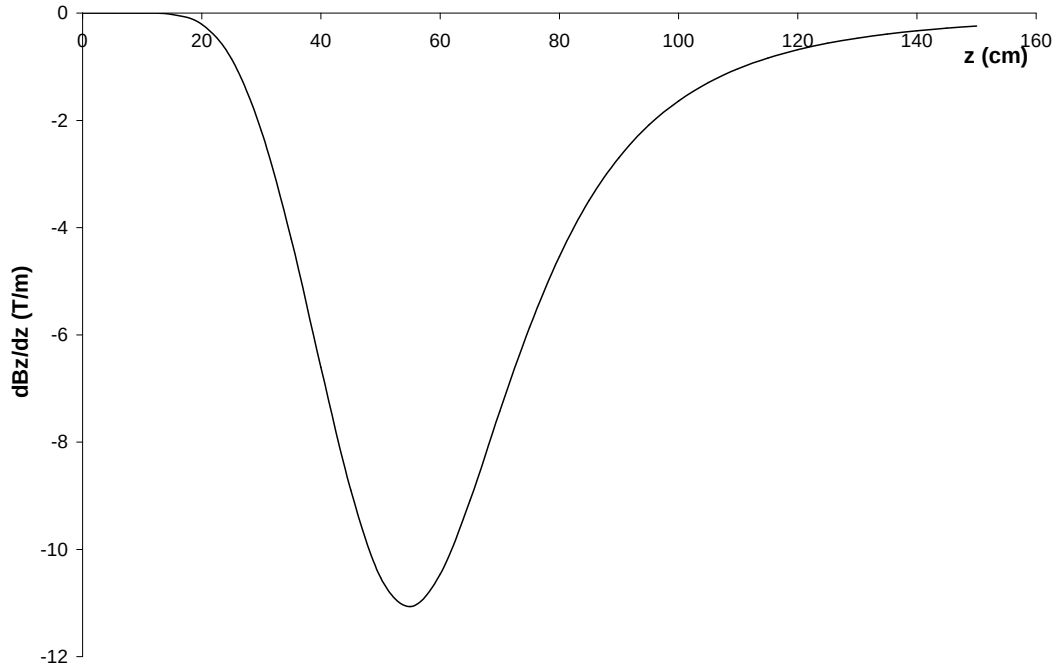

Figure 4.11 – Magnetic field gradient (T/m) with respect to *z* along the *z*-axis (cm)

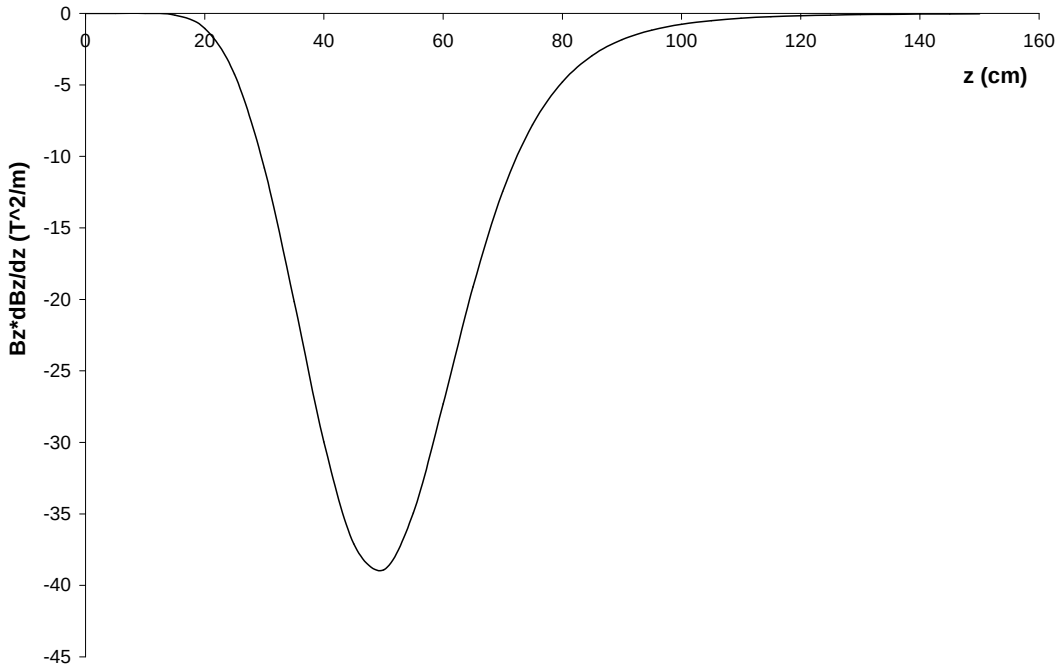

Figure 4.12 – Product of the magnetic field in the *z*-direction and the magnetic field gradient (T^2/m) with respect to *z* along the *z*-axis (cm)

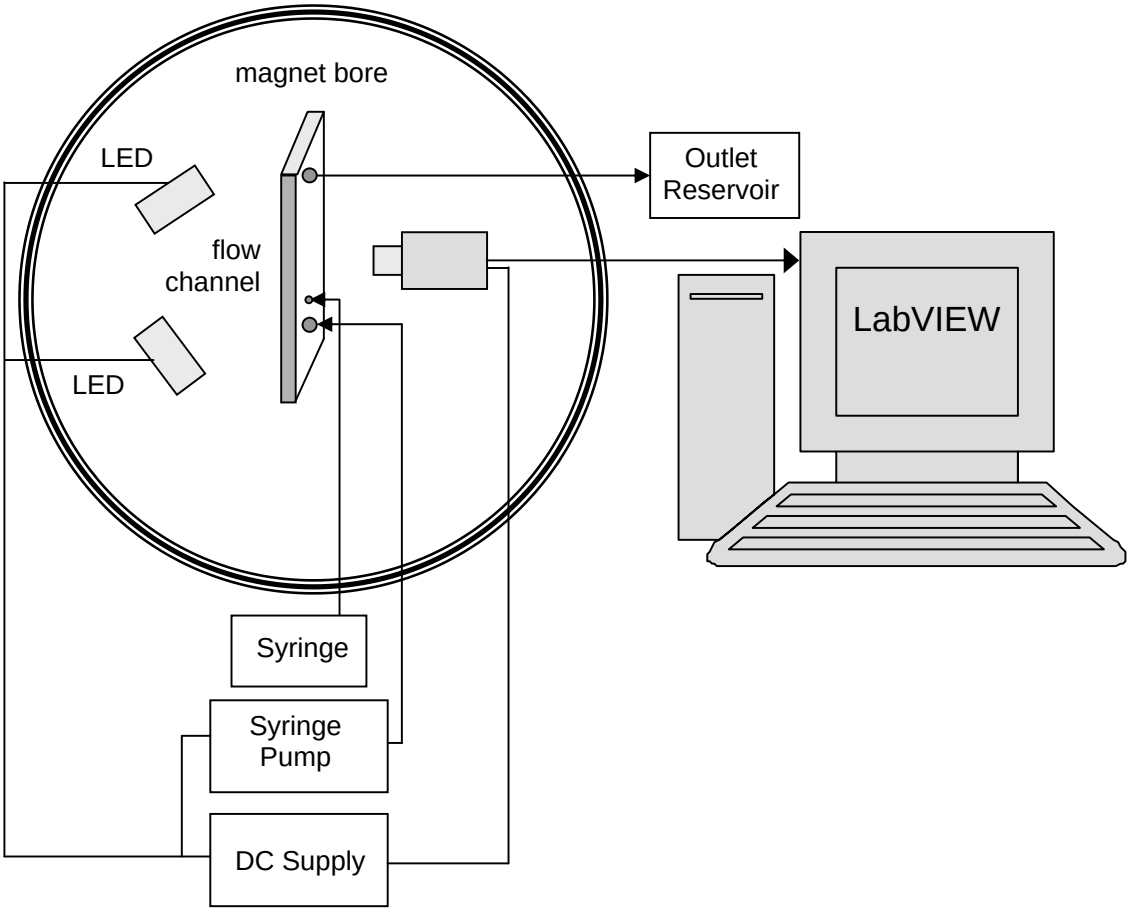

Figure 4.13 – Diagram of the flow and data collection system

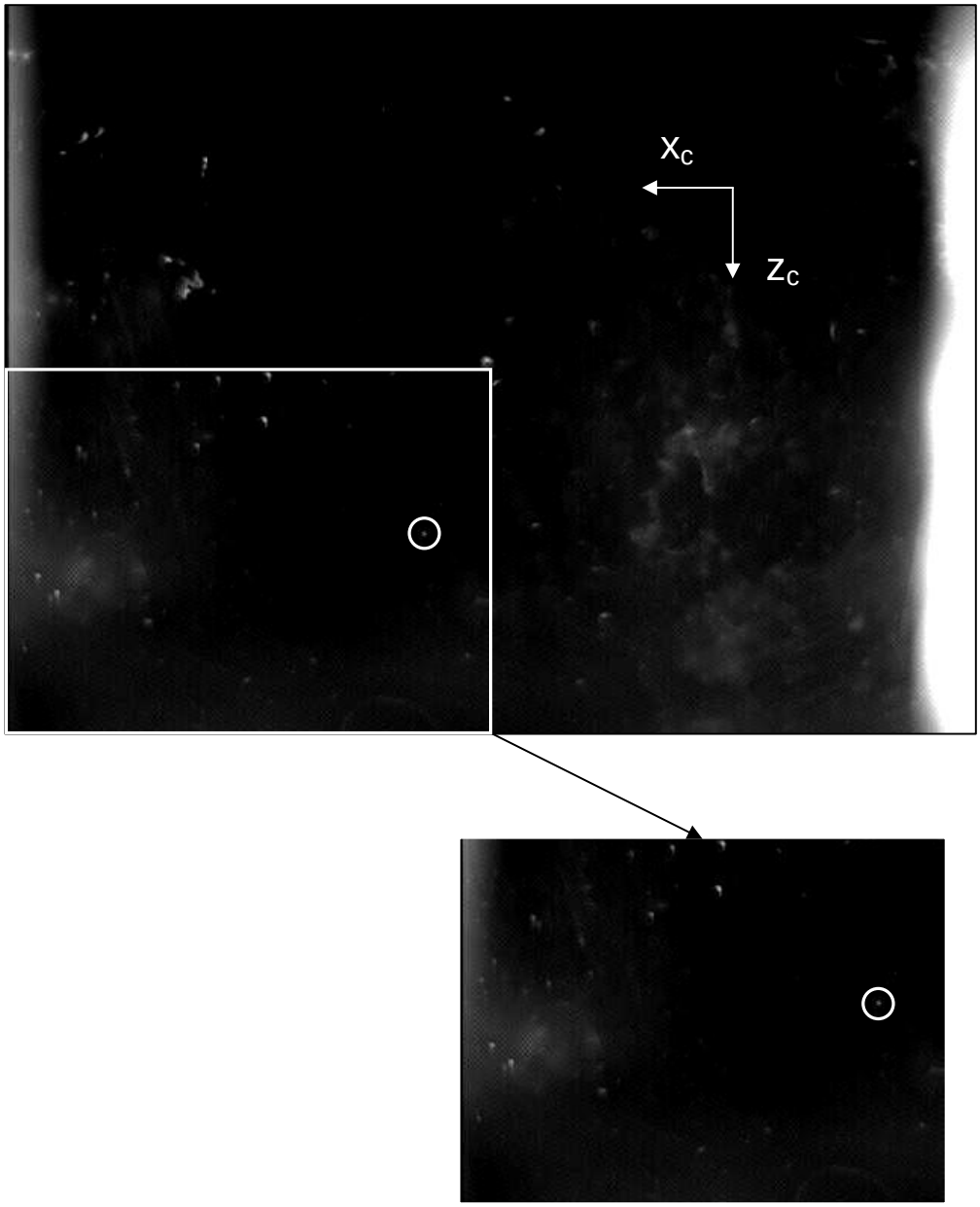

Figure 4.14 – An image collected by LabVIEW illustrating the zoomed-in section used in Figure 4.8

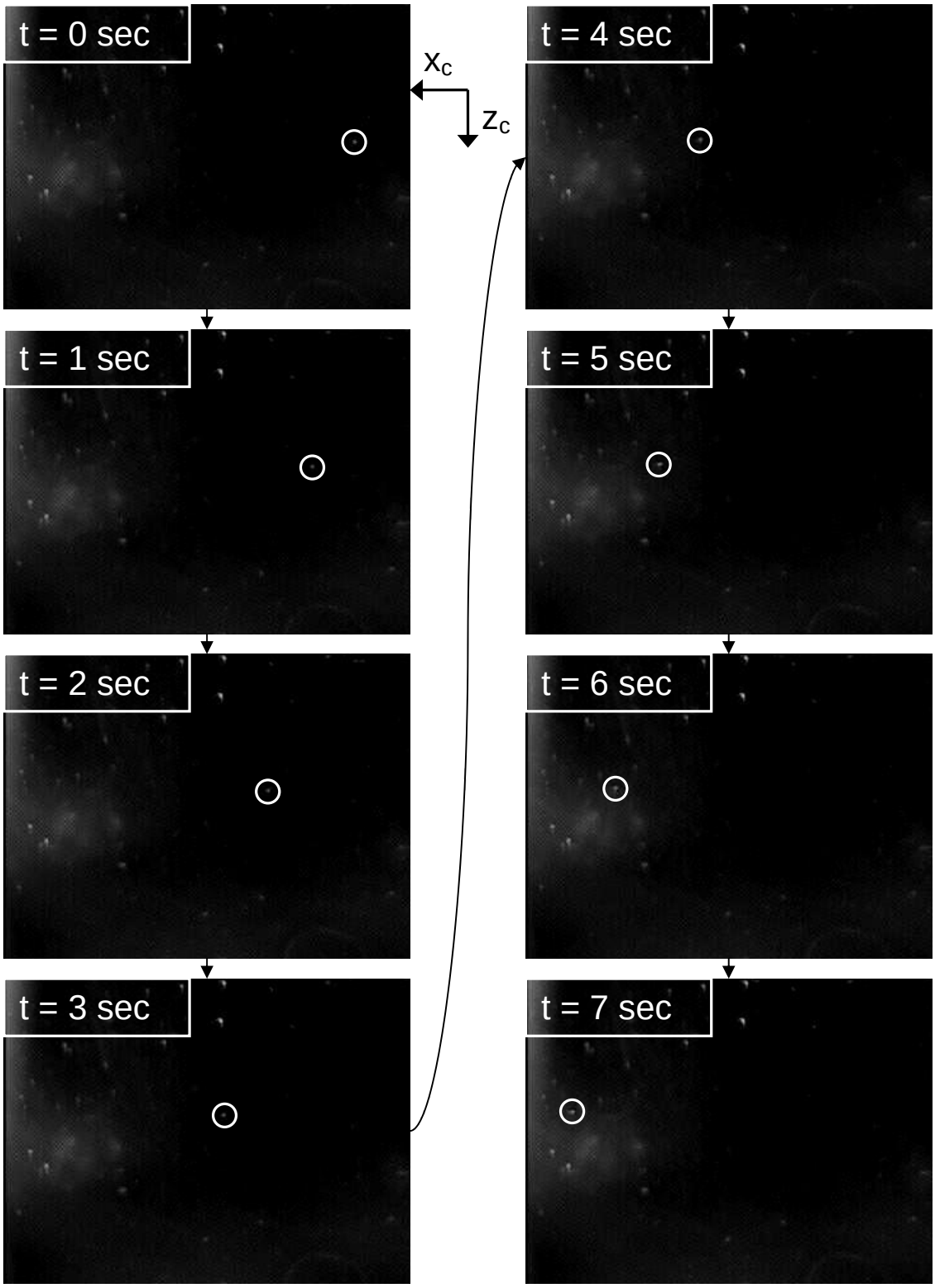

Figure 4.15 – 8 images illustrating the tracking of a particle through a time correlated sequence of images

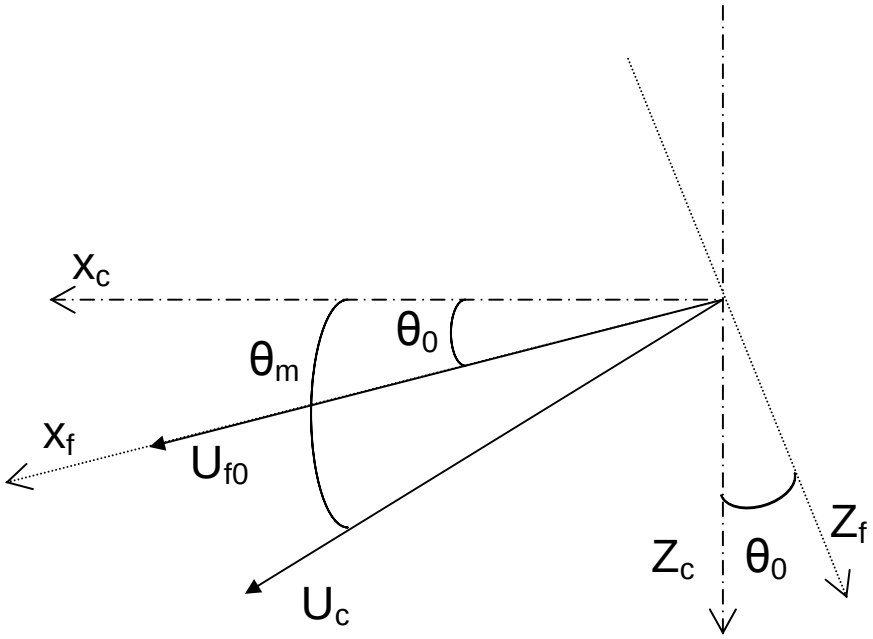

Figure 4.16 – Vector diagram of the flow velocity U_{f0} and particle velocity U_c

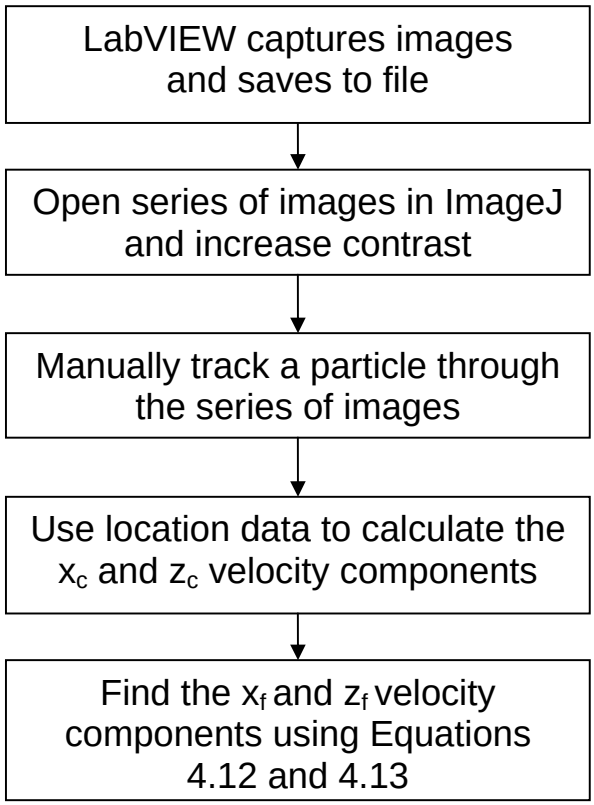

Figure 4.17 – Flow chart detailing the data collection and analyzing process

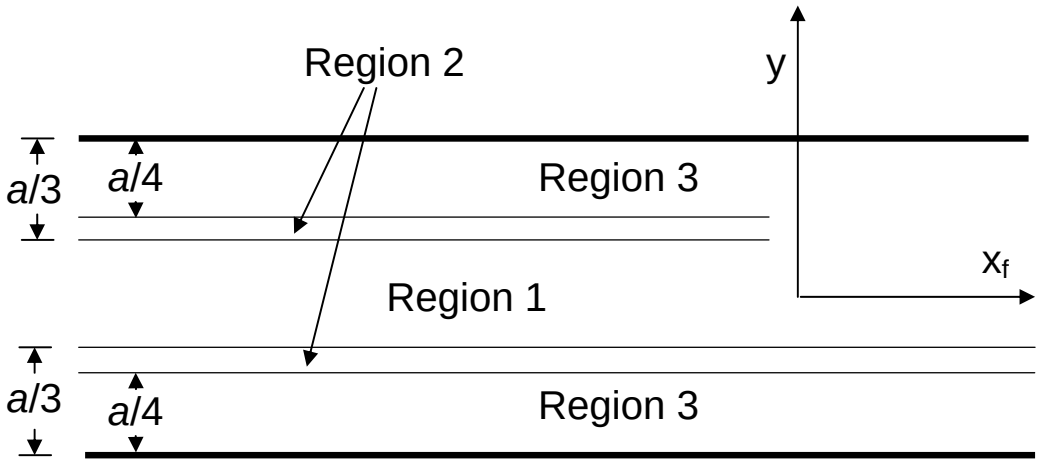

Figure 4.18 – Channel cross-section visually indicating regions used to determine drag coefficient values

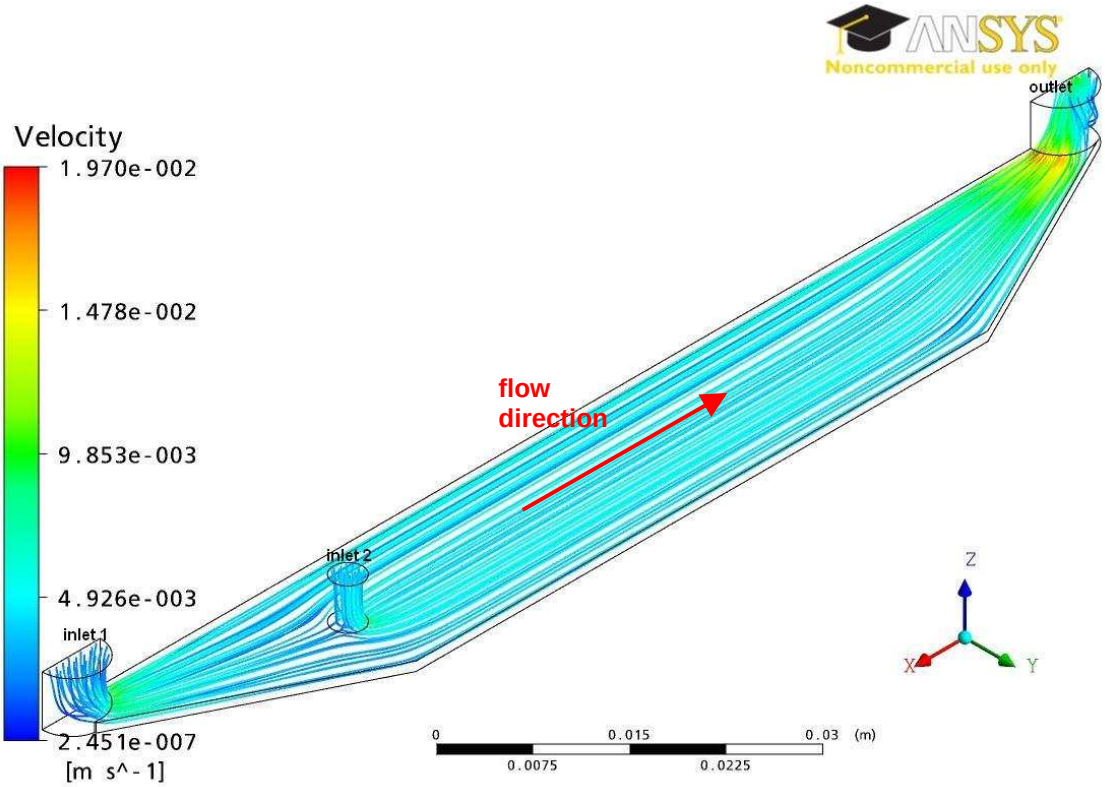

Figure 4.19 - ANSYS-CFX modeling of the fluid flow through the channel illustrating the laminar flow streamlines

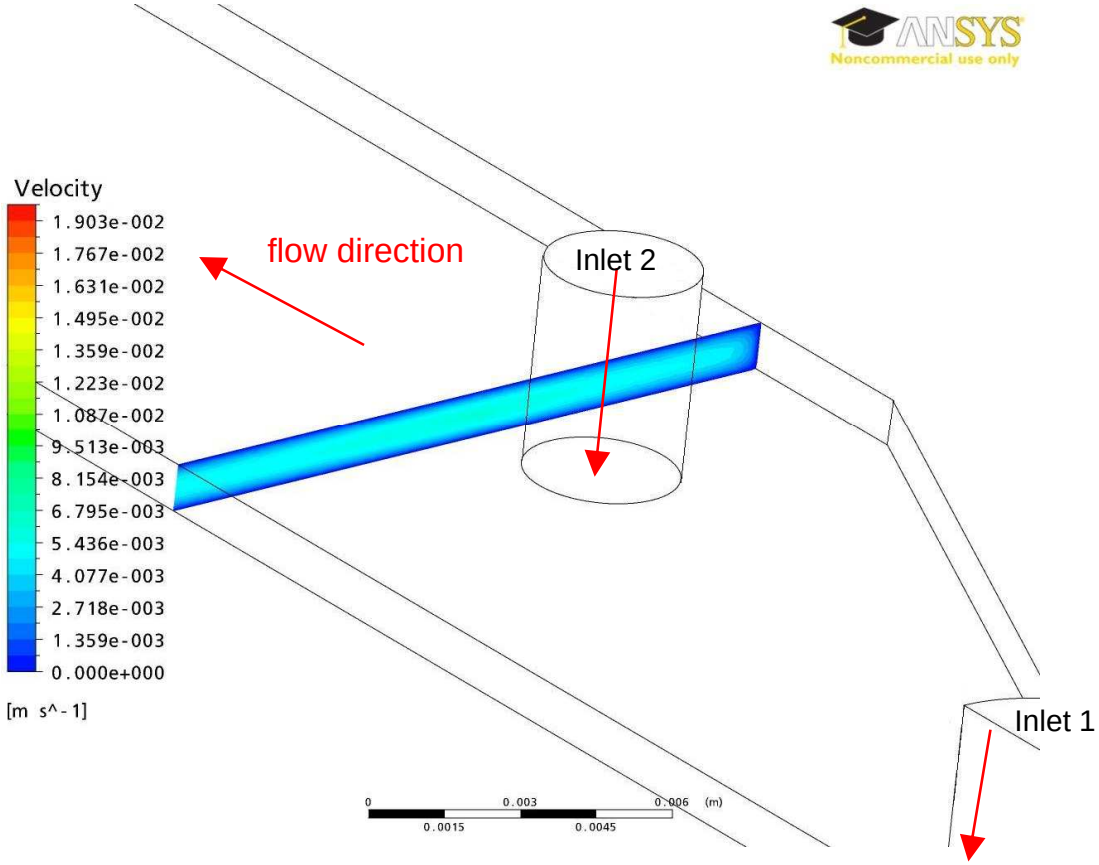

Figure 4.20 –ANSYS-CFX modeling of the fluid flow through the channel illustrating the laminar flow cross-section shortly after the sample input

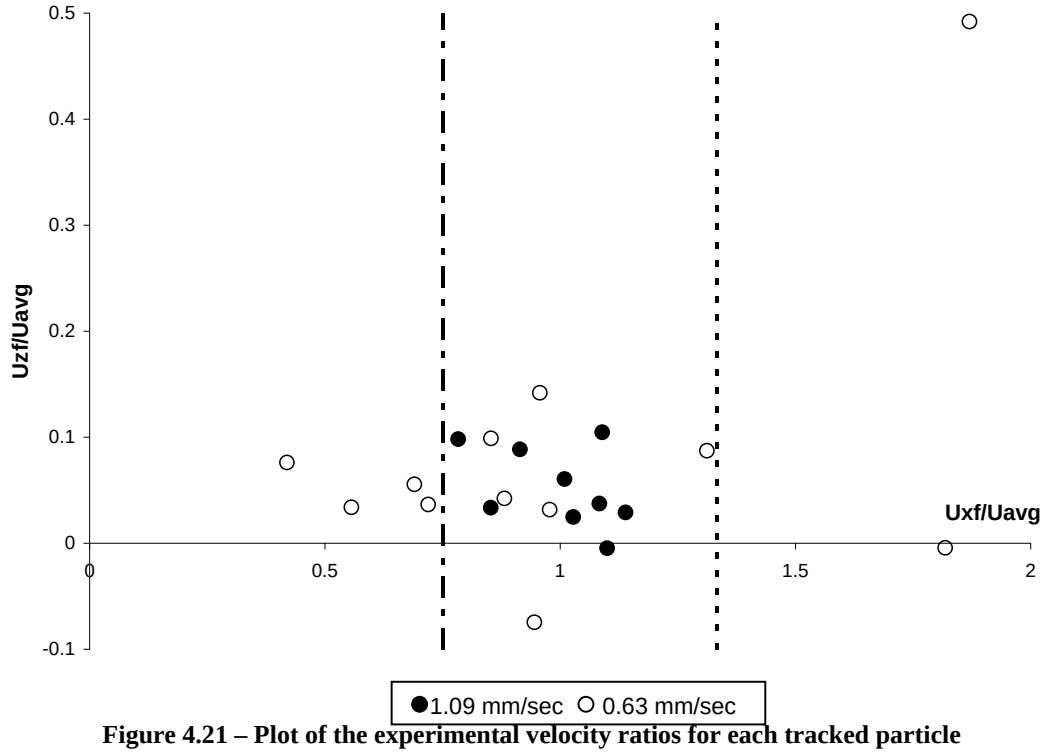

Figure 4.21 – Plot of the experimental velocity ratios for each tracked particle where *a* = 1.18 mm. Data gathered for two different syringe pump rates resulting in average particle velocities of 0.63 and 1.09 mm/sec.

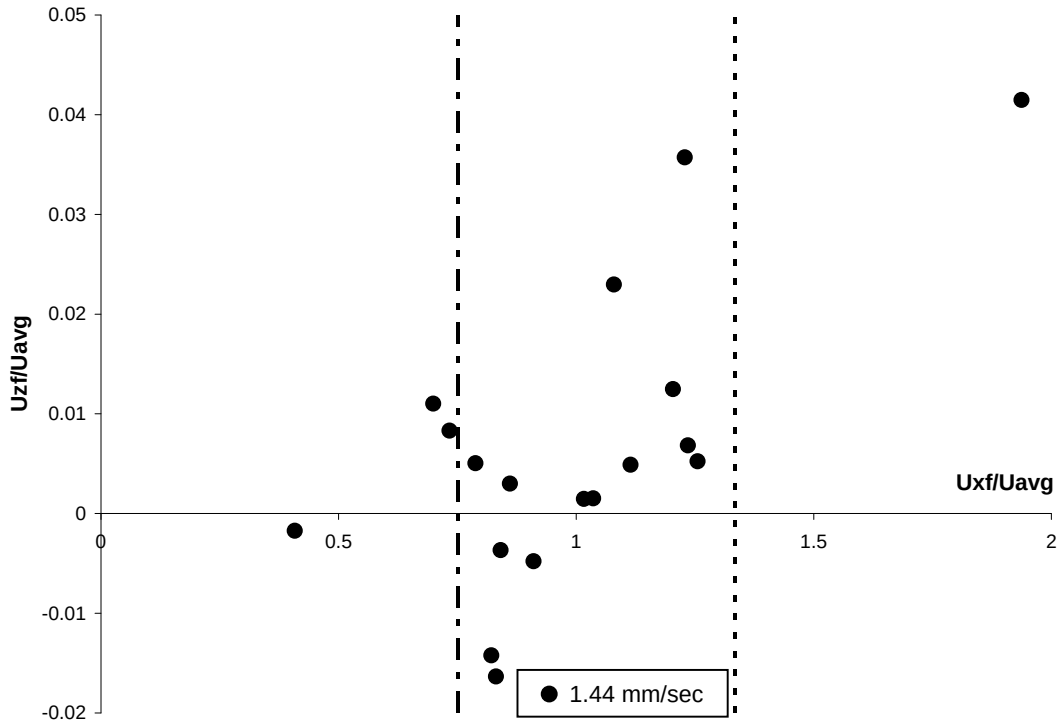

Figure 4.22 - Plot of the experimental velocity ratios for each tracked particle where *a* = 0.254 mm and 1.44 mm/sec average particle velocity

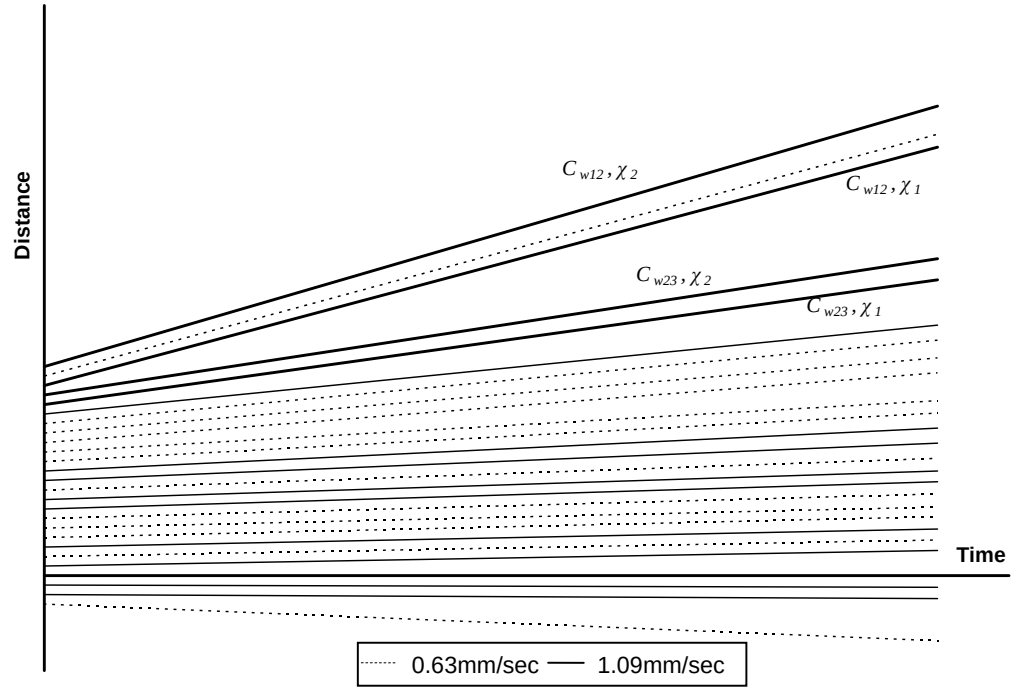

Figure 4.23 –Plot of the particle displacement due to the magnetic force vs. time for flow through a channel with thickness 1.18 mm. The thick solid lines indicate the expected slopes for drag coefficient and magnetic susceptibility values as labeled.

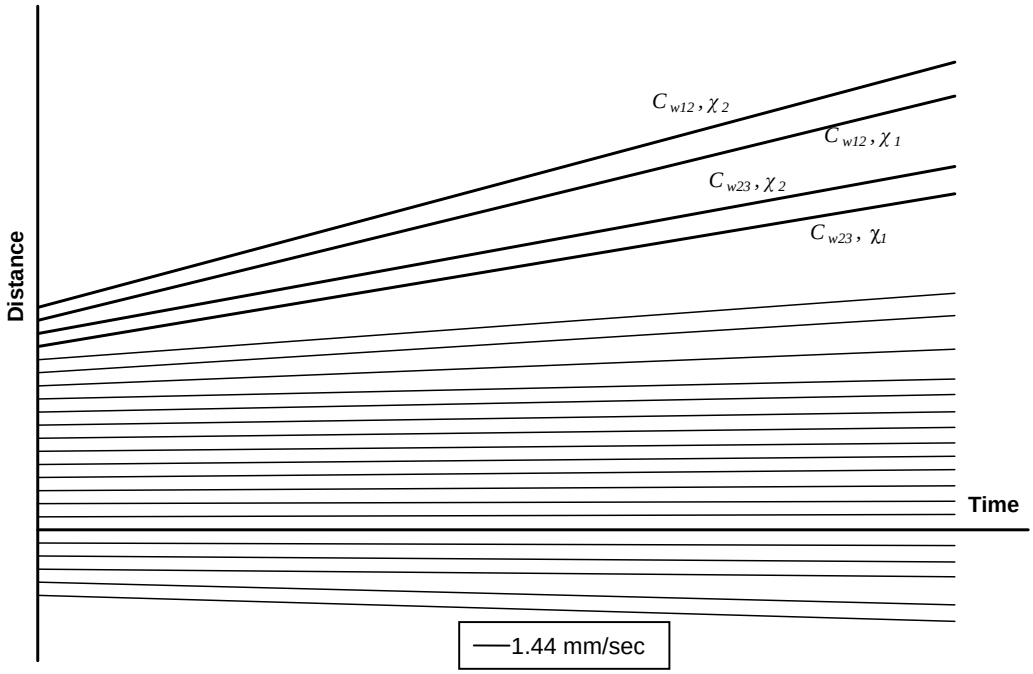

Figure 4.24 - Plot of the particle displacement due to the magnetic force vs. time for flow through a channel with thickness 0.254 mm. The thick solid lines indicate the expected slopes for drag coefficient and magnetic susceptibility values as labeled.

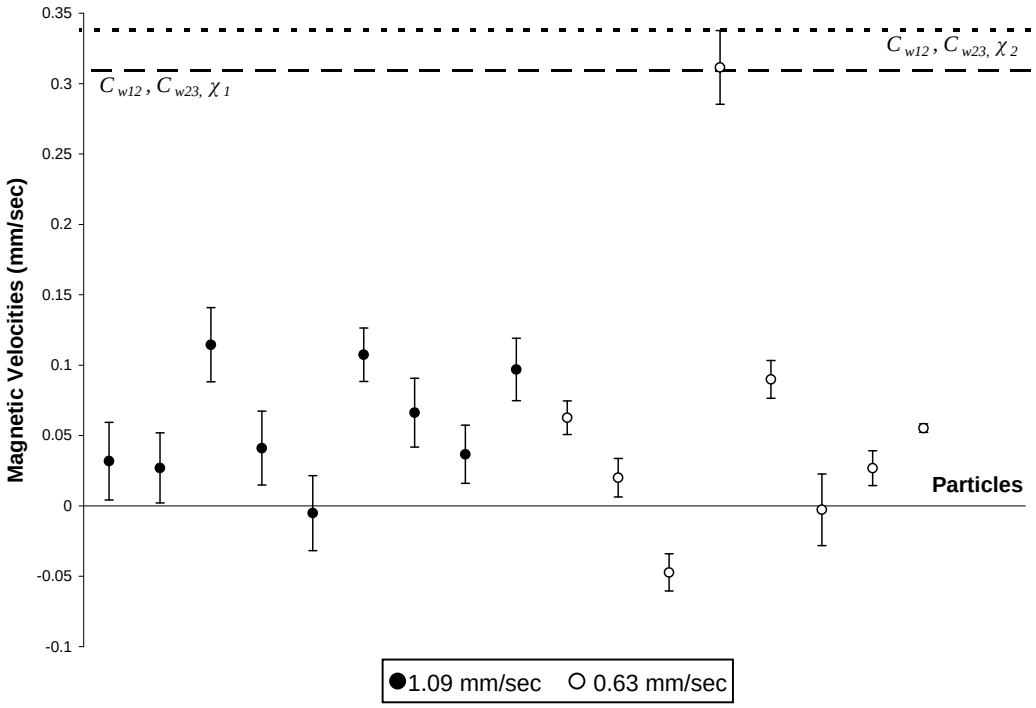

Figure 4.25 –Plot of the magnetic velocities for each particle including error bars shown in comparison to the expected velocities where a = 1.18mm and r/a = 0.043 for 1.09 and 0.63 mm/sec average flow velocities

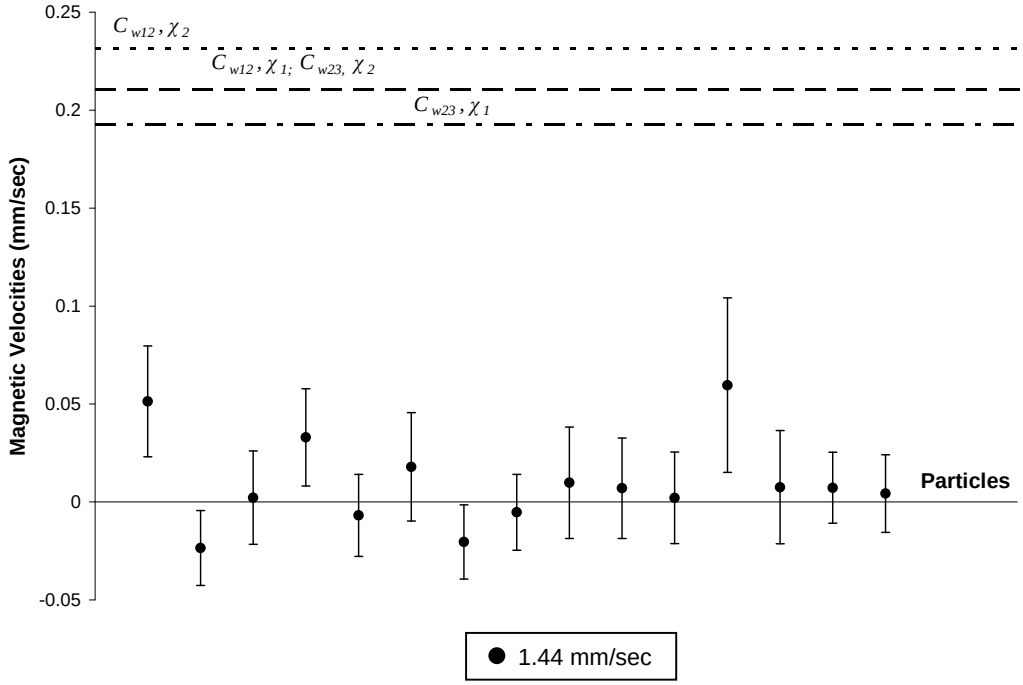

Figure 4.26 - Plot of the magnetic velocities for each particle including error bars shown in comparison to the expected velocities where a = 0.254 mm and r/a = 0.199 for a 1.44mm/sec average flow velocity

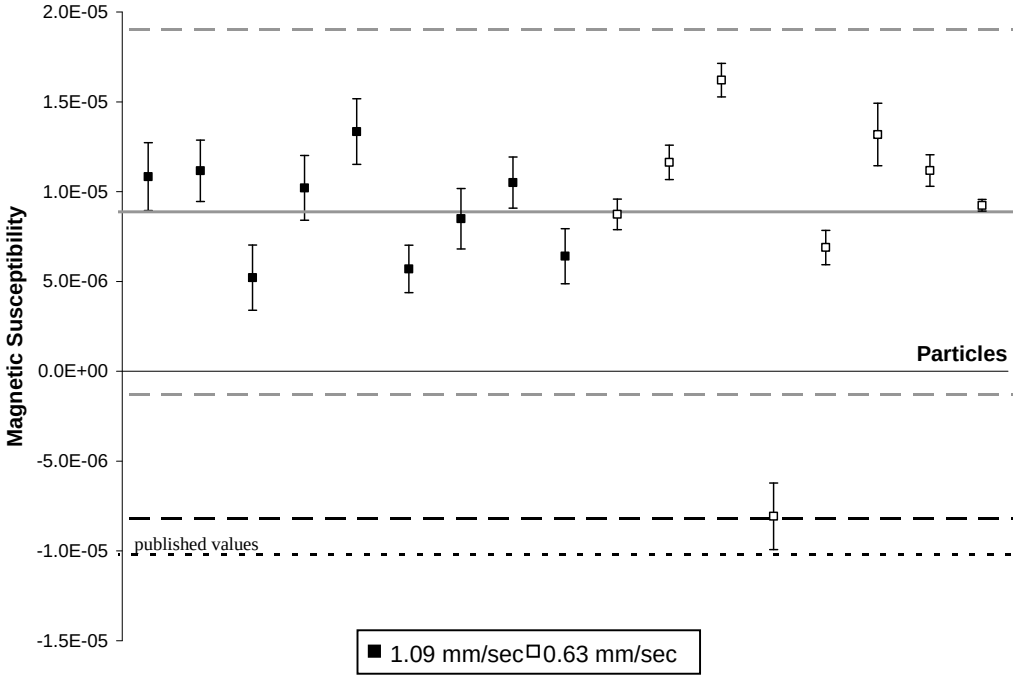

Figure 4.27 – Plot of the experimental magnetic susceptibilities, including error bars, calculated from the magnetic velocities for a = 1.18 mm and r/a = 0.043. The grey lines indicate the average ± 2 standard deviations.

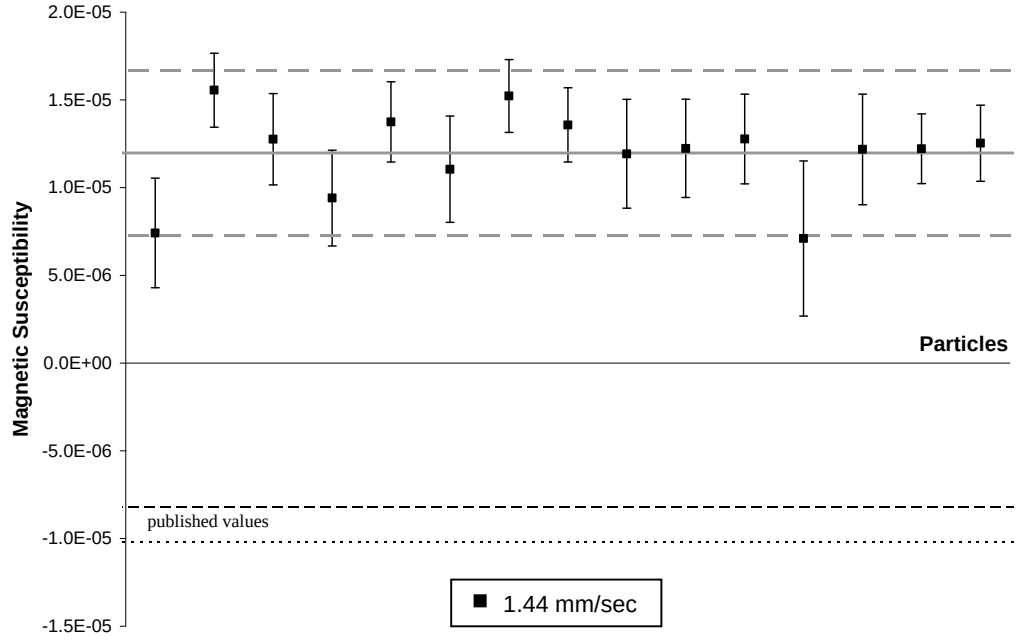

Figure 4.28 – Plot of the experimental magnetic susceptibilities, including error bars, calculated from the magnetic velocities for a = 0.254mm and d/a = 0.199. The grey lines indicate the average ± 2 standard deviations.

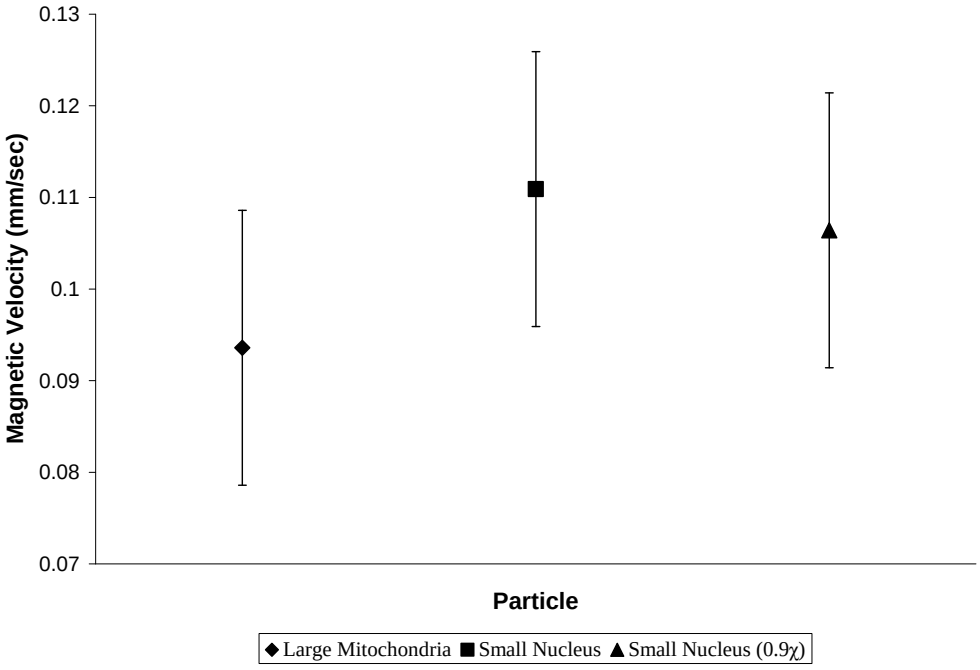

Figure 4.29 – Plot of possible subcellular organelle magnetic velocities corresponding to Table 4.7 with experimentally determined uncertainty of 0.015 mm/sec

Table 4.1 - Values used to calculate the experimental magnetic susceptibilities from Equation 4.9

Property	Value	Units	Source
$\bar{\chi}_{fl}$	1.30E-05	-	Equation 4.9
η	1.11E-03	kg/m·sec	Phang 1980
r_p	50.5	μm	manufacturer (Polysciences, Inc.)
B	3.696	T	Figure 4.6
dB/dz	-10.528	T/m	Figure 4.7
μ_0	4π x 10^{-7}	N/A^2	vacuum permeability
a_A	1.18	mm	measured
$\overline{C}_{w12A}$	1.0924	-	average of calculations from Eqns 4.3 and 4.4
$\overline{C}_{w23A}$	1.0985	-	average of calculations from Eqns 4.3 and 4.4
a_B	0.254	mm	measured
$\overline{C}_{w12B}$	1.5985	-	average of calculations from Eqns 4.3 and 4.4
$\overline{C}_{w23B}$	1.7577	-	average of calculations from Eqns 4.3 and 4.4

Table 4.2 – Representative uncertainty contributions for one particle

$\left\lvert \frac{\eta r C_w U_{zf}}{V_p \left(B \frac{dB}{dz} \right)^2} \right\rvert^2 \Delta \left(B \frac{dB}{dz} \right)^2 = 2.53x10^{-15}$
$\left\lvert \frac{\eta C_w U_{zf}}{B \frac{dB}{dz}} \left(\frac{3}{8\pi r^3} \right) \right\rvert^2 \Delta r^2 = 3.27x10^{-18}$
$\left\lvert \frac{r C_w U_{zf}}{V_p B \frac{dB}{dz}} \right\rvert^2 \Delta \eta^2 = 7.72x10^{-21}$
$\Delta \bar{\chi}_{fl}^{\ 2} = 5.34x10^{-14}$
$\left\lvert \frac{\eta r C_w}{V_p B \frac{dB}{dz}} \right\rvert^2 \Delta U_{zf}^{\ 2} = 3.51x10^{-12}$
$\left\lvert \frac{\eta r U_{zf}}{V_p B \frac{dB}{dz}} \right\rvert^2 \Delta C_w^{\ 2} = 2.12x10^{-16}$

Table 4.3 – Angular offsets calculated for all possible combinations of particle magnetic susceptibility and drag coefficient, for a = 1.18 mm

Inputs	Φ (radians)	Φ (degrees)
C_{w12}, χ_1	0.076	4.358
C_{w12}, χ_2	0.082	4.696
C_{w23}, χ_1	0.076	4.361
C_{w23}, χ_2	0.082	4.700
Average Φ	0.079	4.529

Table 4.4 - Angular offsets calculated for all possible combinations of particle magnetic susceptibility and drag coefficient, for a = 0.254 mm

Inputs	Φ (radians)	Φ (degrees)
C_{w12}, χ_1	0.067	3.818
C_{w12}, χ_2	0.073	4.157
C_{w23}, χ_1	0.067	3.835
C_{w23}, χ_2	0.073	4.173
Average Φ	0.070	3.996

Table 4.5 – Theorized magnetic velocities for a = 0.254 mm, B*dB/dz = -38.91 T^2/m

Particle	d (μm)	r/a	$\overline{\chi}$	U_{zf} (μm/sec)	U_{zf} (mm/sec)
polymer	50	0.099	-8.21E-06	80.57	0.081
polymer	101	0.199	-8.21E-06	322.11	0.322
small nucleus	11	0.022	-9.05E-06	4.12	0.004
large nucleus	22	0.044	-9.05E-06	16.40	0.016
small mitochondria	1	0.002	-9.05E-06	0.03	3E-05
large mitochondria	10	0.020	-9.05E-06	3.40	0.003
ribosome	0.02	0.000	-9.05E-06	1.37E-05	1.37E-08

Table 4.6 –Theorized magnetic velocities for a =55μm and two different magnetic fields: B*dB/dz = -38.91 T^2/m and B*dB/dz = -1300 T^2/m

		B*dB/dz=-38.91T^2/m		B*dB/dz=-1300T^2/m	
Particle	r/a	U_{zf} (μm/sec)	U_{zf} (mm/sec)	U_{zf} (μm/sec)	U_{zf} (mm/sec)
small nucleus	0.100	3.33	0.003	111.198	0.111
large nucleus	0.200	10.31	0.01	344.578	0.345
small mitochondria	0.009	0.034	3.40E-05	1.121	0.001
large mitochondria	0.091	2.81	0.003	93.871	0.094
ribosome	0.000	1.37E-05	1.37E-08	4.57E-04	4.57E-07

Table 4.7 – Comparison of magnetic velocities produced by particles very close in size and magnetic susceptibility

Particle	d (μm)	$\overline{\chi}$	U_{zf} (mm/sec)
small nucleus	11	-9.05E-06	0.1109
large mitochondria	10	-9.05E-06	0.0936
small nucleus, $\overline{\chi}$	11	-9.05E-06	0.1109
small nucleus, 0.9* $\overline{\chi}$	11	-8.15E-06	0.1064

5. Summary

In this study two techniques, vibrating microcantilever beams and magnetophoresis, were experimentally investigated for test specimens to evaluate the sensitivity and accuracy of magnetic susceptibility detection. The investigations allowed for assessment of the techniques' capabilities when applied to subcellular organelles.

Detection of the magnetic susceptibility of subcellular organelles presents a unique challenge for various reasons. Subcellular organelles are nano and micro-scale in size making measurement of size and mass as well as visualization extremely difficult. In addition, the magnetic susceptibility magnitudes are expected to be small (-9.051×10^{-9} m^3/kg) with the expected variation between organelles types on the order of 10%. Both techniques were chosen for their ability to circumvent these issues. When examining resonance frequency shifts of microcantilever beams, particles of interest need not have a known mass and radius or be visually detectable. The implementation of magnetophoresis also does not require a known mass and magnifies the magnetic field effects.

Microcantilever beam tests examined resonance frequency shifts using a bismuth test particle ($m = 7.88 \times 10^{-5}$ kg) on the tip of a silicon microcantilever beams (L = 5mm, b = 2mm, t = 20-50 μm) to establish a detection method uncertainty of 0.013 Hz. To determine the technique feasibility for application to subcellular organelles, a theoretical examination of resonance frequency shifts due to the application of a magnetic field was conducted for silicon, silicon nitride and polymer beams of varying dimensions. Results

indicate that only a polymer beam (L = 0.2mm, b = 0.1mm, t = 0.1μm) can produce a detectable resonance frequency shift that is greater than the experimentally determined uncertainty (0.013 Hz). However, to sense the differences in resonance frequency shifts due to a 10% variance in magnetic susceptibility, an uncertainty smaller than 0.009 Hz is required. In summary, the microcantilever beam approach cannot achieve sufficient sensitivity to detect the predicted differences among different subcellular organelle types.

Tests implementing magnetophoresis for polystyrene test particles with a 100μm diameter suggest the technique is promising for application to subcellular organelles. The trial runs explored different flow speeds of 0.63, 1.09, and 1.44 mm/sec using a manganese chloride and water solution as well as particle radius to channel depth ratios (r/a) of 0.043 and 0.199. Results indicate that a larger r/a ratio leads to more consistent flow velocities and calculated magnetic susceptibilities. Results of the flow speed examination indicate that faster flow speeds lead to more consistent flow velocities but a slower flow speed leads to smaller magnetic velocity and susceptibility uncertainties. The trial runs indicate that a balance of a larger d/a ratio and a slower flow speed is ideal to optimize consistency in flow velocities and calculated magnetic susceptibilities while minimizing uncertainty.

The trial runs also indicate several adaptations to the process and apparatus are recommended to ensure success. The larger $B*\mathrm{d}B/\mathrm{d}z$ created by the 17T superconducting magnet is necessary to generate more accurate magnetic velocity detection, as such the apparatus including the mounting device and flow channel must be redesigned to fit within the much smaller 50mm radius bore. When the flow direction is parallel to the gravitational force vector ($\Phi = 0$), mass is no longer a factor in the calculation of

magnetic susceptibility and the magnetic velocities are maximized. Therefore the design should feature a 'level' of sorts to ensure proper alignment. Rotation of the channel orientation so that the flow direction is perpendicular to the gravitational force vector is another option that achieves the same purpose. The current approach, which relies on visual detection, will not be adequate for small diameter samples. Since one pixel corresponds to 31μm, the current visualization technique can only detect particles larger than 31μm. Since even the largest subcellular organelle, the nucleus, is estimated to be 22 μm, the current microscope camera apparatus would not be adequate to track the movement of subcellular organelles. Potential solutions that must be explored for viability include a higher-quality CCD camera, fluorescent tagging, and laser light scattering. The visualization process is further complicated by the fact that it must enable real-time tracking of the particle and be magnetic field tolerant. An additional obstacle to magnetophoresis implementation is the similar size of the experimental magnetic susceptibility uncertainty and the expected magnetic susceptibility variance by organelle type. When implemented, all of the preceding recommendations should contribute to a reduction in uncertainty.

6. References

Ali, S. M., Mantell, S. C., and Longmire, E. K., 2006, "Reliability of Microcantilevers in Liquid Environments," SPIE Conference on Reliability, Packaging, Testing, and Characterization of MEMS/MOEMS V, San Jose, CA.

Calleja, M., Nordstrom, M., Alvarez, M., 2005, "Highly Sensitive Polymer-Based Cantilever-Sensors for DNA Detection," Ultramicroscopy, **105**(1) pp. 215-222.

Cowin, S. C., 1998, "On Mechanosensation in Bone Under Microgravity," Bimechanics and Mechanical Sensing, **22**(5) pp. 119-125.

Finot, E., Thundat, T., Lesniewska, E., 2001, "Measuring Magnetic Susceptibilities of Nanogram Quantities of Materials using Microcantilevers," Ultramicroscopy, **86**(1) pp. 175-180.

Happel, J., and Brenner, H., 1973, "Low Reynolds Number Hydrodynamics,"Noordhoff International Publishing, Leyden, The Netherlands, pp. 322-331, Chap. 7.

Iiguni, Y., Suwa, M., and Watarai, H., 2004, "High-Magnetic-Field Electromagnetophoresis of Micro-Particles in a Capillary Flow System," Journal of Chromatography A, **1032**(1) pp. 165-171.

Iwasaka, M., Miyakoshi, J., and Ueno, S., 2001, "Magnetophoresis of Diamagnetic Cells and Microorganisms in a Culture Medium," IEEE Transactions on Magnetics, **37**(4) pp. 2644-2646.

Karolik, V. A., and Zhuk, I. P., 1979, "Experimental Study of the Temperature Dependence of the Magnetic Susceptibility of Certain Nematic Liquid Crystals and their Mixtures," Journal of Engineering Physics and Thermophysics, **37**(2) pp. 979-981.

Kawaguchi, H., 2000, "Functional Polymer Microspheres," Progress in Polymer Science, **25**(8) pp. 1171-1210.

Kuehn, T. P., Ali, S. M., Mantell, S. C., 2007, "Testing Reliability of MEMS Materials in Liquids," Proceedings of SPIE, Reliability, Packaging, Testing and Characterization of MEMS/MOEMS VI, San Jose, CA.

Lavrik, N. V., Sepaniak, M. J., and Datskos, P. G., 2004, "Cantilever Transducers as a Platform for Chemical and Biological Sensors," Review of Scientific Instruments, **75**(7) pp. 2229-53.

Lim, C. T., Zhou, E. H., and Quek, S. T., 2006, "Mechanical Models for Living Cells - A Review," Journal of Biomechanics, **39**(2) pp. 195-216.

Pamme, N., and Wilhelm, C., 2006, "Continuous Sorting of Magnetic Cells Via on-Chip Free-Flow Magnetophoresis," Lab on a Chip, **6**(8) pp. 974-980.

Phang, S., 1980, "The Density, Viscosity and Transference Number of Aqueous Manganese Chloride at 298.15 K," Australian Journal of Chemistry, **33** pp. 413.

Tanimoto, Y., Fujiwara, M., Sueda, M., 2005, "Magnetic Levitation of Plastic Chips: Applications for Magnetic Susceptibility Measurement and Magnetic Separation," Japanese Journal of Applied Physics, **44**(9A) pp. 6801-6803.

Tarn, M. D., Hirota, N., Iles, A., 2009, "On-Chip Diamagnetic Repulsion in Continuous Flow," Science and Technology of Advanced Materials, **10**(1) pp. 014611.

van Loon, J. J. W. A., 2007, "Micro-Gravity and Mechanomics," Gravitational and Space Biology, **20**(2) pp. 3-18.

Appendix A : Evaluation of Finot Paper Results

Evaluation of the Finot et al. (2001) results is necessary to determine if their data could be re-created using the system presented in this paper. It will also provide guidance as to why their experiment produced quantifiable results while this paper could not. The resonance frequency shifts produced and the magnetic field used in the Finot study are of particular interest.

Using information given in the Finot paper, values for f_s and $f_{s,m}$ can be calculated for comparison. The Finot paper gives a beam stiffness of 35 mN/m, a beam resonance frequency f_0 of 16 KHz, a maximum force gradient of 0.01 N/m, and a ErO_3 sample mass of 1.58×10^{-12} kg. To find values for f_s and $f_{s,m,}$ the mass of the beam (1.47×10^{-11} kg) is first calculated from Equation 3.2. Using Equation 3.3, a theoretical resonance frequency of the beam with the mass on the tip f_s of 13.3 kHz is calculated. A value for $f_{s,m}$ of 15.04 kHz is calculated from Equation 3.4. The differences between f_0, f_s and $f_{s,m}$ are all detectable for the system proposed in this paper.

The much larger resonance frequency shifts could be due a much large magnetic field and gradient product. While the Finot paper does not provide a magnetic field or gradient, the given maximum force gradient (0.01 N/m) and Equation 3.5 result in a magnetic field gradient on the order of 10^6 T/m. This value is much larger than the maximum gradient presented in this paper of 143 T/m. As a result, a larger magnetic field and gradient led to detectable results in the Finot study.

<u>Appendix B:</u> Magnetophoresis Uncertainty Calculation

The absolute error of calculated magnetic susceptibility due to the uncertainty of the components is computed using the partial derivative approach

$$\Delta X^2 = \left|\frac{\delta f}{\delta A}\right|^2 \Delta A^2 + \left|\frac{\delta f}{\delta B}\right|^2 \Delta B^2 + \left|\frac{\delta f}{\delta C}\right|^2 \Delta C^2 + \ldots \tag{B.1}$$

where $X = f(A, B, C\ldots)$. When Equation B.1 is applied to Equation 4.8, the absolute error of the magnetic susceptibility is

$$\Delta\chi_p^2 = \left|\frac{rC_w U_{zf}}{V_p B \frac{dB}{dz}}\right|^2 \Delta\eta^2 + \Delta\bar{\chi}_{fl}^2 + \left|\frac{\eta C_w U_{zf}}{B\frac{dB}{dz}}\left(\frac{3}{8\pi r^3}\right)\right|^2 \Delta r^2 + \left|\frac{\eta r U_{zf}}{V_p B \frac{dB}{dz}}\right|^2 \Delta C_w^2 + \ldots$$

$$\ldots + \left|\frac{\eta r C_w}{V_p B \frac{dB}{dz}}\right|^2 \Delta U_{zf}^2 + \left|\frac{\eta r C_w U_{zf}}{V_p\left(B\frac{dB}{dz}\right)^2}\right|^2 \Delta\left(B\frac{dB}{dz}\right)^2. \tag{B.2}$$

The contributions to the error from each component are treated separately. The error contribution from the magnetic field value is due to the uncertainty of the particle position in the magnet bore. The camera's field of view is approximately 2 centimeters wide and the placement of the camera and flow channel is potentially off the target location by 0.5 cm in either direction. The value of $B(dB/dz)$ at the optimal location (z = 50cm) is -38.91 T^2/m. The values of $B(dB/dz)$ at locations z_1 = 45cm and z_2 = 55cm are -37.09 T^2/m and -34.93 T^2/m. The rate of change of $B(dB/dz)$ in the direction of z_2 is 0.7959 $T^2/m \cdot cm$ and in the direction of z_1 is 0.36482 $T^2/m \cdot cm$. Since $B(dB/dz)$ increases in different amounts in both directions, only the maximum rate of change will be used to

find the error contribution. The particles can be located at z = 50cm ± 1.25cm so the rate of change is multiplied by 1.25cm. As a result, $\Delta B(dB/dz)$ is 0.995 T^2/m.

The error contribution from the particle size is given by the manufacturer. The diameter of the particle is indicated to be 101.63 ± 0.17 μm.

The C_w error contribution is due to the uncertainty in particle location in the channel as well as limitations due to the C_w values for three discrete channel locations. As described in Section 4.3, the channel is divided into 3 regions (see Figure 4.17) into which the particles are separated. The average C_{w1} and C_{w2} is used as the drag coefficient for particles in region 1. The drag coefficient uncertainty ΔC_{w12} is half the difference of C_{w1} and C_{w2}

$$\Delta C_{w12} = \frac{C_{W2} - C_{W1}}{2}. \qquad \text{(B.2)}$$

For region 2, the process is repeated with C_{w2} and C_{w3}

$$\Delta C_{w23} = \frac{C_{W3} - C_{W2}}{2}. \qquad \text{(B.3)}$$

The thick channel dimensions produce ΔC_{w12} and ΔC_{w23} values of 0.0013 and 0.0074. The thin channel dimensions produce ΔC_{w12} and ΔC_{w23} values of 0.0128 and 0.1464.

The viscosity and fluid magnetic susceptibility error contributions are due to mixing and measuring errors. The solution was consistently mixed with 500mL ± 25mL of water and 0.05405kg ± 0.001kg of manganese chloride. A trendline is fit to viscosity values of a $MnCl_2$ solution for discrete molalities to give an equation of viscosity as a function of molality (mol of solute/kg solvent) (Phang 1980). The molality of the experimental solution is 0.137 mol/kg resulting in a viscosity of 9.47×10^{-4} kg/m·sec. Due to the uncertainties from mixing and measuring, the molality uncertainty is 1.26×10^{-4}

mol/kg. The error in viscosity $\Delta\eta$ is half of the difference between the viscosity values for the maximum and minimum possible molalities or 4.47x10^{-8} kg/m·sec. Since the fluid magnetic susceptibility is calculated using Equation 4.9, the error is calculated using Equation B.4

$$\Delta\bar{\chi}_{fl} = \frac{m_M}{(m_M + m_W)^2}\bar{\chi}_W \Delta m_W + \frac{m_W}{(m_M + m_W)^2}\bar{\chi}_M \Delta m_M \qquad \text{(B.4)}$$

where m_W is the mass of water, m_M is the mass of manganese chloride, $\bar{\chi}_W$ is the magnetic susceptibility of water, and $\bar{\chi}_M$ is the magnetic susceptibility of manganese chloride. As a result the fluid magnetic susceptibility error $\Delta\bar{\chi}_{fl}$ is 2.31x10^{-7}.

The magnetic displacement velocity error contribution is due to measurement of the pixels per millimeter conversion, accuracy of the velocity measurement technique, and accuracy of the x_f-z_f and x_c-z_c coordinate system transformation. Since the pixels per millimeter conversion factor was found by measuring the conversion factor for the front and the back of the glass plates, the error is half of the difference between the two factors or 2.876 pixels/mm for the thick channel and 2.410 pixels/mm for the thin channel. To determine the accuracy of the velocity measurement technique, the process detailed in the Figure 4.13 flow chart is repeated five times for five different particle movements. The particle paths chosen varied in speed and visibility quality. The standard deviation σ of the five different velocities for each particle was multiplied by two to give the uncertainty U per particle ($U = 2\sigma$). All five uncertainties were averaged to give a total velocity uncertainty of 3.24x10^{-4} pixels/sec. The value was then divided by the conversion factor ± the conversion factor error and the two results were then averaged to 9.99x10^{-6} mm/sec (thick) and 9.58x10^{-6} mm/sec (thin). The contribution of the coordinate system

transformation to the magnetic velocity error is important as well. The x_f axis for the thick and thin channel separately was calculated as an average angle from multiple particle velocities with an uncertainty of twice the standard deviation. The thick channel angle uncertainty is 0.022 radians or 1.27 degrees. The thin channel angle uncertainty is 0.016 radians or 0.94 degrees. For each particle velocity measured in the magnetic field, an individual uncertainty is calculated by taking half the difference of the x_f-z_f coordinate plane velocities found using the maximum and minimum possible angles. The uncertainty contribution from the pixels/mm conversion and the velocity detection technique are added to the individual uncertainties to give a final ΔU_{zf} for each particle. The averages of the total ΔU_{zf} for each particle are 0.0198 (a = 1.18mm) and 0.0248 (a = 0.254mm) mm/sec. All uncertainty contribution components are detailed in Table B.1.

Table B.1 – Contributions to the magnetic susceptibility error

	Value	Units
$\Delta B(\mathrm{d}B/\mathrm{d}z)$	0.995	T^2/m
Δr_p	0.085	μm
$\Delta \overline{\chi}_{fl}$	2.31E-07	-
$\Delta \overline{C}_{w12A}$	0.0013	-
$\Delta \overline{C}_{w23A}$	0.0074	-
$\Delta \overline{C}_{w12B}$	0.0128	-
$\Delta \overline{C}_{w23B}$	0.1464	-
$\Delta\eta$	4.47E-08	kgm/sec
ΔU_{zfA} (average)	0.0198	mm/sec
ΔU_{zfB} (average)	0.0248	mm/sec

Appendix C: Supplementary Data Gathered for Different Bore Locations

This section presents data gathered at different locations within the superconducting magnet and provides comparison between using paramagnetic and diamagnetic fluids. The values of the magnetic field and gradient product at discrete locations are shown in Figure C.1.

Particle velocity data was gathered at locations z = 20 , 30, 40, and 50 cm corresponding to magnetic field and gradient products of -1.05, -10.88, -29.96, and -38.91 T^2/m using the paramagnetic solution described in Section 4.2. After performing the required x_c-z_c to x_f-z_f coordinate transformations, the magnetic velocities U_{zf} are plotted with respect to z-location in Figure C.2. The figure also includes the expected velocities calculated for the locations using both published polystyrene magnetic susceptibility values. The plot suggests that the measured magnetic velocities are much smaller than their expected counterparts.

Figure C.3 plots the magnetic velocities with respect to the magnetic field and gradient product. The relationship between the magnetic velocity and the magnetic field and gradient product is theoretically linear, evidenced by the two lines created using the published magnetic susceptibility values. This plot further demonstrates that the expected and experimental patterns do not correlate. The discrepancy is a result of differing angles Φ between the x-z and x_f-z_f coordinate systems at different locations. The process of moving the apparatus to a different location within the bore allows for potential changes to the orientation due to the lack of complete stability.

The magnetic susceptibilities calculated from the velocities at all four locations are plotted in Figure C.4 along with the published values. It is interesting to note that the values become much more varied as the magnetic field decreases. Magnetic susceptibilities calculated from data taken at the same four locations using water (a diamagnetic fluid) are plotted in Figure C.5. The same pattern of increased variation due to decreased magnetic field is present. The data was gathered for comparison purposes. However, due to potential Φ differences at different locations, no meaningful comparison analyses can be gleaned from this data.

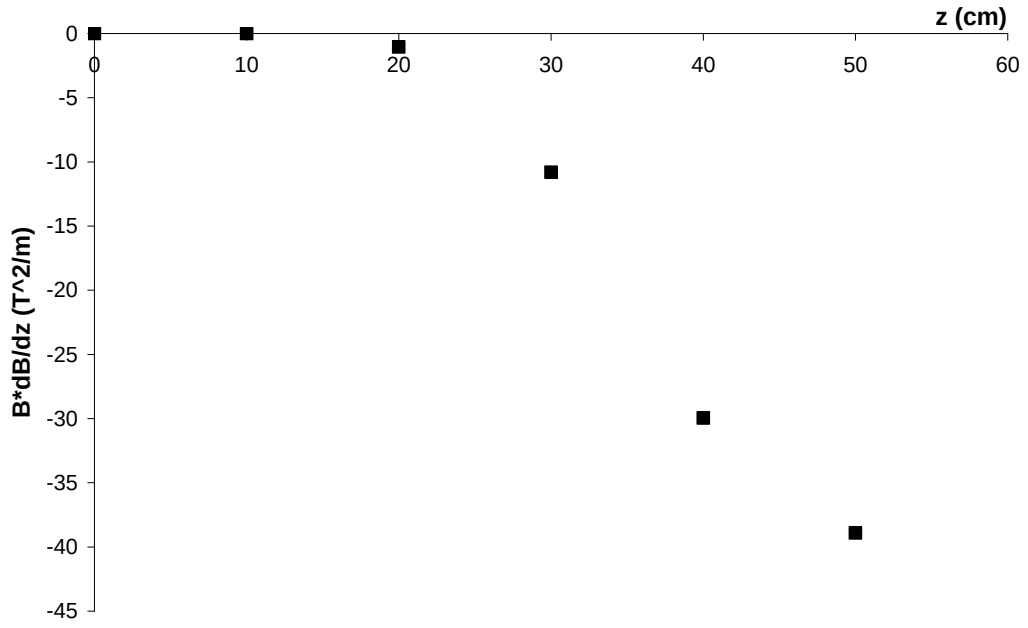

Figure C.1 – Plot of the magnetic field and gradient product at the discrete locations for which data is gathered

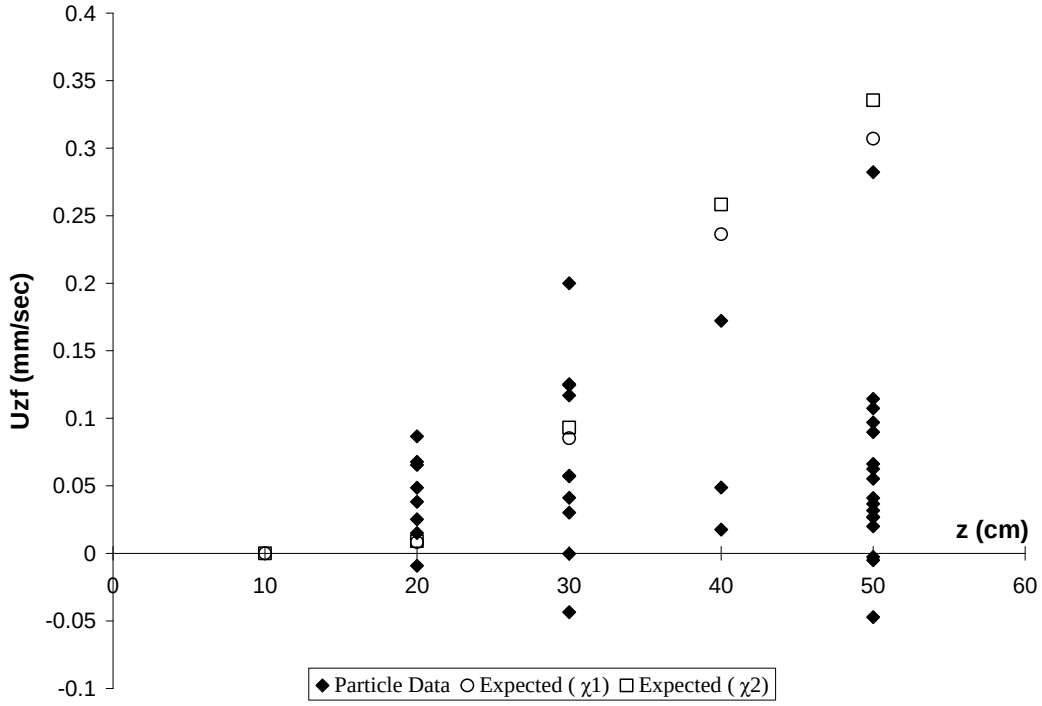

Figure C.2 – Plot of the magnetic velocities U_{zf} for all particles gathered at 4 locations with the expected velocities indicated

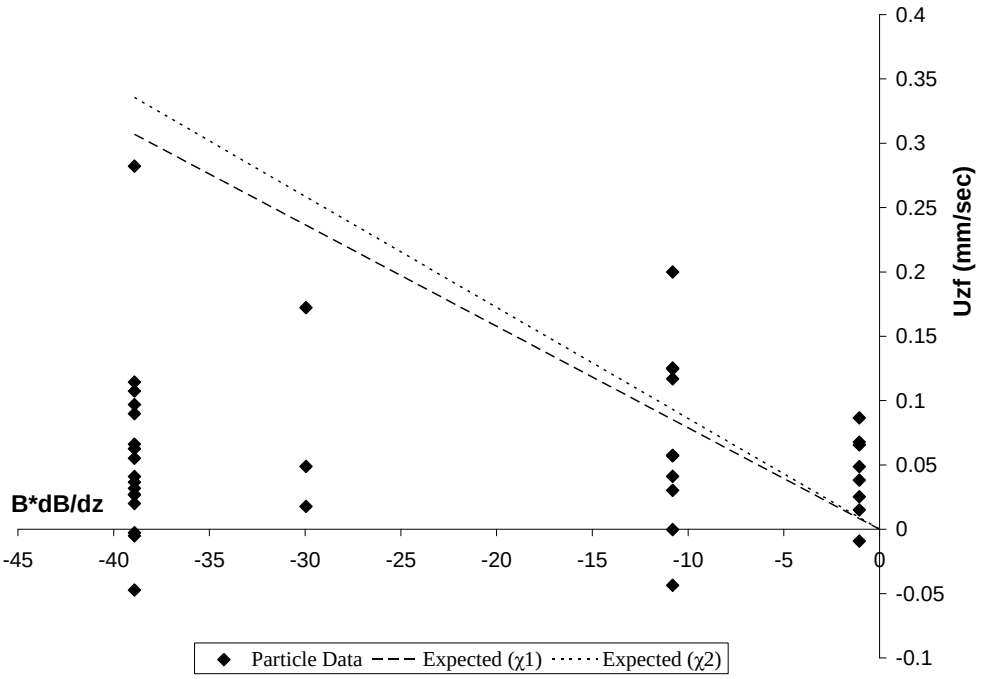

Figure C.3 – Magnetic velocities plotted against the magnetic field and gradient product. The expected linear relationship is included

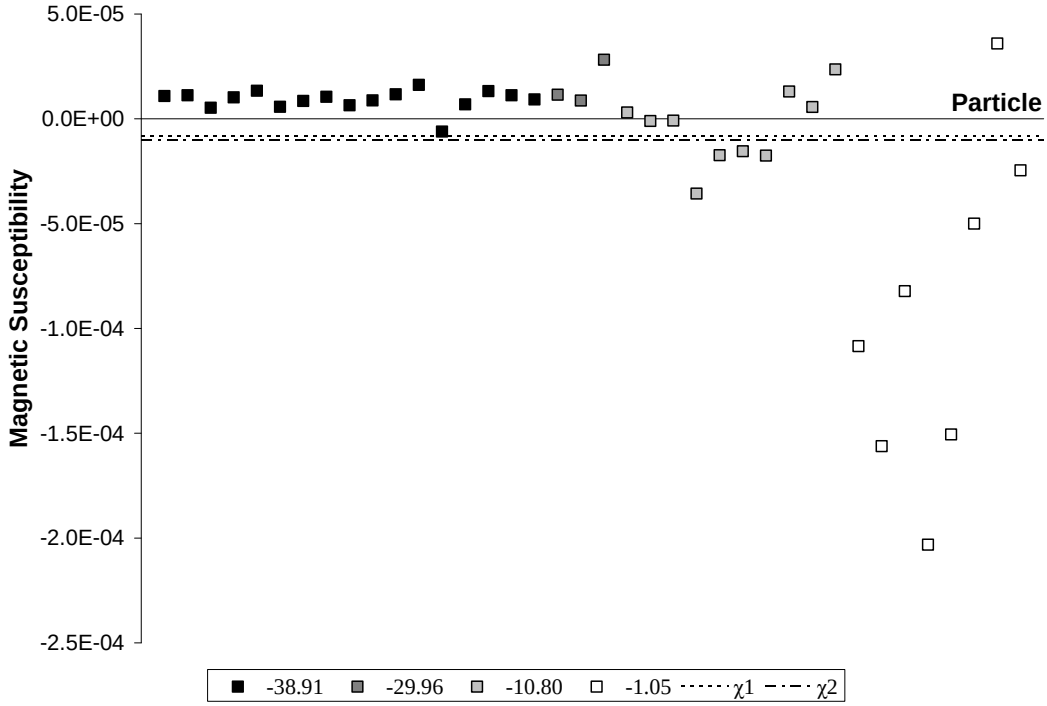

Figure C.4 – Plot of the magnetic susceptibilities calculated from the velocities measured for four different magnetic field and gradient products using the paramagnetic fluid along with the published magnetic susceptibility values

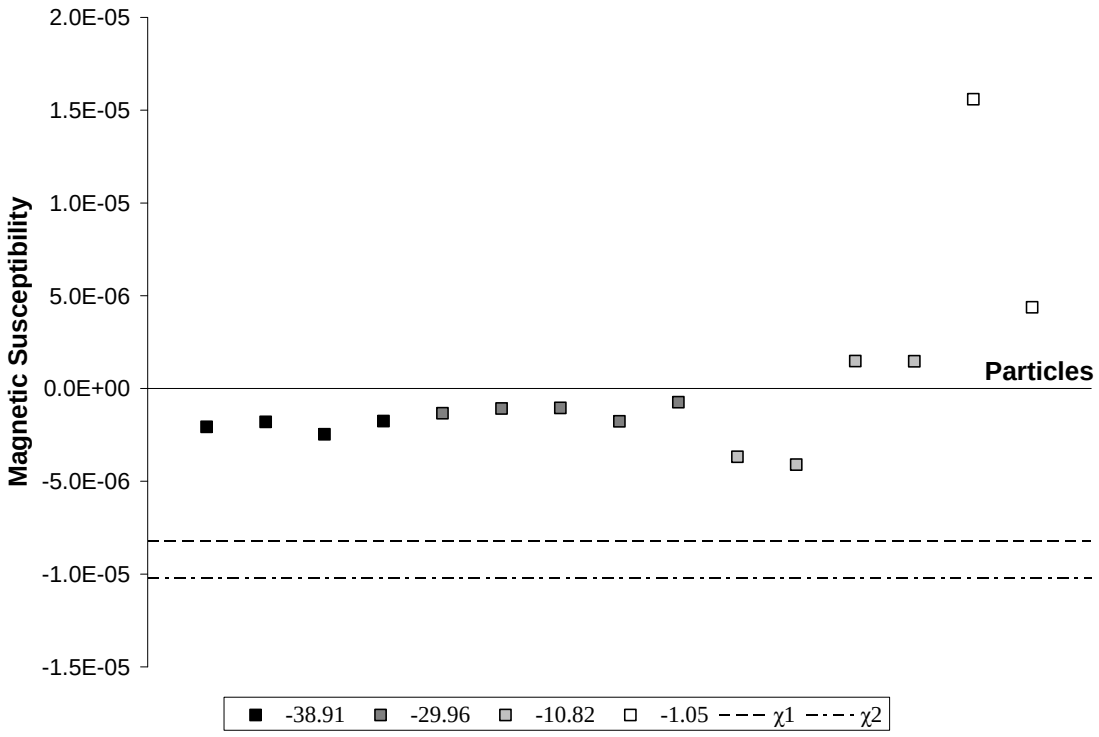

Figure C.5 – Plot of the magnetic susceptibilities calculated from the velocities measured for four different magnetic field and gradient products using water along with the published magnetic susceptibility values